PREFACE TO THE EDITION

It is with great pleasure and a profound sense of responsibility that we present the inaugural issue of the **Eduschool Journal of Environmental Research Studies (EJERS)**. At a time when environmental challenges are increasingly shaping global policy, scientific inquiry, and societal priorities, this journal seeks to provide a scholarly platform for advancing knowledge, fostering interdisciplinary dialogue, and promoting evidence-based solutions for a sustainable future.

The first issue of EJERS brings together a collection of research articles that illuminate critical dimensions of contemporary environmental change. Collectively, these contributions underscore the interconnectedness of Earth's climate systems, ecosystems, and human activities while highlighting the urgent need for informed environmental stewardship.

The opening article examines the *Atlantic Meridional Overturning Circulation (AMOC) and the growing risk of climate tipping points* associated with its weakening. By exploring future projections and collapse thresholds, the study offers important insights into the far-reaching consequences that disruptions in large-scale ocean circulation may have on global climate stability, regional weather patterns, and sea-level dynamics.

Addressing the challenge of climate mitigation within rapidly expanding urban environments, the second contribution evaluates the *carbon sequestration potential of urban green infrastructure.* Through a comprehensive lifecycle assessment across tropical megacities, the study demonstrates how carefully planned urban ecosystems can contribute meaningfully to carbon management while enhancing environmental resilience.

The third article focuses on the increasingly significant issue of *permafrost thaw and* methane *emissions*. By assessing the carbon feedbacks associated with Arctic warming, the study highlights the potential for substantial greenhouse gas releases from thawing permafrost and emphasizes the implications for global carbon budgets and international climate targets.

Extending the discussion of natural climate solutions, the fourth contribution investigates *blue carbon storage in mangrove–seagrass ecotones*. By quantifying carbon stocks within these transitional coastal habitats, the research reveals an often-overlooked carbon reservoir and reinforces the importance of conserving coastal ecosystems as part of broader climate mitigation strategies.

The issue concludes with an analysis of *land-use change and carbon emissions in Southeast Asia*, a region that remains one of the world's most dynamic environmental frontiers. Through its examination of deforestation trends, policy interventions, and emission trajectories, the study highlights both the progress achieved and the challenges that remain in balancing economic development with environmental sustainability.

Taken together, the articles in this inaugural issue reflect the multidisciplinary character of environmental research and demonstrate the value of integrating climate science, ecosystem studies, geospatial analysis, and policy evaluation. They remind us that environmental challenges transcend geographical and disciplinary boundaries and require collaborative approaches grounded in rigorous scientific evidence.

We extend our sincere appreciation to the authors for their valuable contributions, the reviewers for their thoughtful evaluations, and the editorial team for their dedication in bringing this first issue to fruition. We also thank our readers and the broader academic community for their support and engagement.

As EJERS begins its journey, we remain committed to promoting high-quality environmental scholarship that informs policy, inspires innovation, and contributes to the global pursuit of ecological sustainability and climate resilience. We hope that this inaugural issue serves as both a meaningful contribution to environmental discourse and a foundation for future research endeavors.

Dr. K. Madhusudhanan

Chief editor

`CONTENTS

EDUSCHOOL JOURNAL OF ENVIRONMENTAL RESEARCH STUDIES (EJERS)

(Open Access, Double-Blind Peer Reviewed Journal)

ISSN Online:

Atlantic Overturning Circulation And Climate Tipping Points

Dr. Jeeva Chacko

Principal, Department of Zoology, St. Mary's Arts and Science College, Cherupanathady, India.

Article information

Received: 5th March 2026
Received in revised form: 8th April 2026
Accepted: 12th May 2026
Available online: 15th June 2026

Volume: 1
Issue: 1
DOI: https://doi.org/10.5281/zenodo.20696369

Abstract

The Atlantic Meridional Overturning Circulation (AMOC) transports approximately 1.3 PW of heat northward, sustaining the relative warmth of western Europe and influencing precipitation patterns across the tropics and subtropics. Multiple observational and proxy lines of evidence suggest that the AMOC has weakened over recent decades, raising concerns about a potential approach to a critical tipping point beyond which collapse could become irreversible. This study analyzes AMOC projections from eight CMIP6 Earth system models under the SSP5-8.5 scenario, finding a multi-model mean decline of 38 percent by 2100, from 17.7 Sv to 10.9 Sv. Bifurcation analysis applied to three models with freshwater hosing experiments reveals estimated collapse thresholds at 0.28 to 0.32 Sv of anomalous freshwater forcing, with hysteresis widths of 0.12 to 0.18 Sv indicating that recovery from a collapsed state would require substantially greater cooling than the warming that triggered the transition. Two of three analyzed models indicate a high risk of crossing the tipping point by 2100 under unmitigated emissions, with cascading consequences including northern European cooling, southward shift of the Intertropical Convergence Zone, disruption of West African and South Asian monsoons, and accelerated sea-level rise along the North American east coast.

Keywords:- AMOC, Tipping Points, Climate Change, CMIP6, Thermohaline Circulation, Bifurcation

I. INTRODUCTION

The Atlantic Meridional Overturning Circulation is the system of ocean currents that carries warm, saline surface waters northward through the Atlantic basin, where they release heat to the atmosphere, increase in density through cooling and evaporation, and sink to depth in the Nordic Seas and Labrador Sea to form North Atlantic Deep Water11. This deep water flows southward along the western boundary of the Atlantic at depths of 1,500 to 4,000 meters, completing the overturning cell. The AMOC transports approximately 1.3 petawatts of heat across the equator roughly 25 percent of the total poleward heat transport by the combined ocean-atmosphere system making it a fundamental regulator of Northern Hemisphere climate (Rahmstorf, 2002; Buckley & Marshall, 2016).

Paleoclimate evidence from ice cores, ocean sediment records, and speleothems documents multiple episodes of abrupt AMOC weakening or collapse during the last glacial period, notably the Younger Dryas cold reversal (12,900–11,700 years before present) and Heinrich events, during which massive iceberg discharges introduced freshwater pulses that disrupted deep-water formation (Rahmstorf, 2002). These past reorganizations were accompanied by rapid climate shifts temperature changes of 5 to 10°Cover Greenland within decades and global-scale teleconnections including southward displacement of the Intertropical Convergence Zone and disruption of Asian monsoon systems (Rahmstorf, 2002; Jackson et al., 2015).

Contemporary observations have raised alarms that the AMOC may be weakening under anthropogenic forcing. Caesar and colleagues reconstructed AMOC strength using a proxy index based on North Atlantic sea-surface temperature anomalies and found a decline of approximately 15 percent since the mid-twentieth century Caesar et al., 2018). Direct measurements from the RAPID-MOCHA monitoring array at 26.5°N, operational since 2004, recorded a statistically significant decline in AMOC transport of 2.7 Sv between 2004 and 2017, though the short observational record makes it difficult to distinguish trends from decadal variability (Smeed et al., 2018). Boers applied statistical early-warning indicators to multiple AMOC proxy datasets and detected a progressive loss of dynamical stability consistent with an approach toward a

tipping point (Boers, 2021). Ditlevsen and Ditlevsen used advanced statistical methods to estimate that AMOC collapse could occur as early as the mid-2030s, though this projection carries substantial uncertainty (Ditlevsen & Ditlevsen, 2023).

This paper evaluates the risk of AMOC tipping under continued high emissions by analyzing projections from eight CMIP6 models and applying bifurcation theory to assess proximity to critical thresholds. We further examine the cascading impacts of AMOC weakening on European climate, tropical precipitation, and coastal sea levels to inform assessment of the consequences should this tipping point be crossed.

II. LITERATURE REVIEW

2.1. AMOC Observational Evidence

The RAPID-MOCHA monitoring array, deployed across the Atlantic at 26.5°N since April 2004, provides the longest continuous record of full-depth AMOC transport. Smeed and colleagues reported that mean AMOC strength during 2008–2012 was approximately 2.7 Sv weaker than during the initial deployment period of 2004–2008, though subsequent years showed partial recovery followed by renewed decline (Smeed et al., 2018). The mean AMOC transport over the full record period is approximately 17 Sv, with substantial seasonal and interannual variability (standard deviation of approximately 4 Sv) that complicates trend detection from direct observations alone.

Indirect evidence for longer-term AMOC weakening comes from proxy reconstructions. Caesar and colleagues developed a fingerprint index based on the observation that AMOC weakening produces a characteristic pattern of sea-surface temperature anomalies: cooling in the subpolar North Atlantic (the so-called 'warming hole') concurrent with warming in the Gulf Stream region (Caesar et al., 2018). Applying this index to instrumental temperature records, they estimated that the AMOC has declined by approximately 3 Sv (roughly 15 percent) since the mid-twentieth century, making it the weakest in at least a millennium based on comparison with paleoclimate proxy compilations. Buckley and Marshall reviewed the full suite of observational constraints on AMOC variability and concluded that while internal variability remains large, the evidence for anthropogenically forced weakening is strengthening (Buckley & Marshall, 2016).

2.2. CMIP6 Projections

Weijer and colleagues conducted a comprehensive review and synthesis of AMOC projections across CMIP5 and CMIP6 model ensembles, finding a robust decline under all warming scenarios but with substantial inter-model spread in both the rate and magnitude of weakening (Weijer et al., 2019). Under the CMIP6 SSP5-8.5 scenario, most models project AMOC declines of 20 to 60 percent by 2100, with no model projecting an outright collapse (defined as AMOC strength below 2 Sv) within the twenty-first century. However, Weijer and colleagues cautioned that the absence of collapse in CMIP6 projections may reflect model deficiencies rather than physical implausibility, as several known processes that could accelerate AMOC weakening including Greenland Ice Sheet melt, Antarctic meltwater influence on Southern Ocean overturning, and mesoscale eddy feedbacks are poorly represented in current models (Weijer et al., 2019; Bakker et al., 2016).

Liu and colleagues used the CESM1 model in a configuration with corrected freshwater transport bias and demonstrated that AMOC collapse could occur under moderate warming levels (approximately 3°C global mean temperature increase) that several CMIP6 models project will be reached well before 2100 under SSP5-8.5 (Liu et al., 2017). This study highlighted that the response of the AMOC to warming is critically sensitive to the background freshwater transport across the southern boundary of the Atlantic, a quantity that most CMIP6 models represent with systematic biases that may suppress collapse dynamics.

2.3. Tipping Point Theory

The theoretical framework for understanding AMOC tipping derives from the pioneering work of Stommel, who demonstrated in 1961 that the thermohaline circulation possesses two stable equilibrium states a 'strong' mode with vigorous overturning driven by temperature gradients and a 'weak' or 'off' mode dominated by salinity gradients separated by a saddle-node bifurcation (Stommel, 1961). At the bifurcation point, a small perturbation in freshwater forcing can trigger an abrupt transition from the strong to the weak state, and the hysteresis inherent in the system means that reversing the transition requires removal of the freshwater perturbation well beyond the original threshold.

Lenton and colleagues identified the AMOC as one of several 'tipping elements' in the Earth's climate system large-scale subsystems that can undergo qualitative state changes in response to small perturbations near critical thresholds (Lenton et al., 2008). Armstrong McKay and colleagues subsequently updated the assessment of tipping point risks and concluded that exceeding 1.5°C global warming could trigger multiple interacting tipping points, with AMOC weakening potentially cascading through effects on the West African monsoon, Amazon rainforest dieback, and Greenland Ice Sheet loss (Armstrong McKay et al., 2022). Boers applied variance and autocorrelation-based early-warning signals to eight proxy records of AMOC strength and detected a statistically significant increase in both indicators over recent decades, consistent with the critical slowing down that precedes a bifurcation transition (Boers, 2021).

2.4. Freshwater Forcing Mechanisms

The primary mechanism by which anthropogenic warming threatens AMOC stability is through freshwater forcing of the North Atlantic deep-water formation regions. Accelerated melting of the Greenland Ice Sheet delivers approximately 270 Gt yr^{-1} of freshwater to the surrounding ocean, with projections under SSP5-8.5 reaching 800 to 1,600 Gt yr^{-1} by 2100 (Bakker et al., 2016; Intergovernmental Panel on Climate Change [IPCC], 2021). This freshwater reduces surface water density in the Labrador and Nordic Seas, weakening the density-driven sinking that powers the overturning. Additional freshwater sources include increased Arctic river discharge (projected to rise by 10 to 20 percent this century), Arctic sea ice melt, and enhanced net precipitation over the North Atlantic driven by a more vigorous hydrological cycle (Bakker et al., 2016).

Bakker and colleagues quantified the sensitivity of AMOC strength to Greenland Ice Sheet melt rates using a coupled model and found that melt rates exceeding 0.1 Sv (approximately 3,150 Gt yr^{-1}) could trigger collapse within decades (Bakker et al., 2016). Mecking and colleagues demonstrated that the sign and magnitude of the net freshwater transport across the southern boundary of the Atlantic at 34°S (the so-called Fov diagnostic) is a critical predictor of whether a given model will exhibit AMOC bistability: negative Fov values indicate a regime where the AMOC could collapse irreversibly, while positive values suggest monostable behavior (Mecking et al., 2017). Most CMIP6 models produce positive Fov values in their historical simulations, potentially biasing them away from collapse dynamics.

III. METHODOLOGY

3.1. Model Selection

Eight CMIP6 Earth system models were selected based on the availability of monthly ocean meridional overturning streamfunction output (variable msftyz or msftmz) under both the historical experiment (1850–2014) and SSP5-8.5 (2015–2100). The selected models CESM2, UKESM1-0-LL, MPI-ESM1-2-HR, GFDL-CM4, CNRM-ESM2-1, EC-Earth3, IPSL-CM6A-LR, and NorESM2-MM represent major modeling centers and span a range of ocean model resolutions (0.25° to 1°), atmospheric resolutions (0.7° to 1.4°), and equilibrium climate sensitivities (2.6 to 5.4°C). One ensemble member per model (r1i1p1f1) was used to ensure comparability.

3.2. AMOC Index Definition

The AMOC index was defined as the maximum value of the Atlantic meridional overturning streamfunction at 26.5°N, consistent with the latitude of the RAPID monitoring array, enabling direct comparison with observational data. Annual mean values were computed from monthly data after removing the seasonal cycle. Historical-period AMOC strength (mean of 1995–2014) was used as the reference baseline for calculating percentage decline. Time series were smoothed with a 10-year running mean for visualization and trend estimation, while unsmoothed annual values were used for statistical tests.

3.3. Bifurcation Analysis Framework

Bifurcation analysis was conducted for three models (CESM2, UKESM1-0-LL, IPSL-CM6A-LR) that had available freshwater hosing experiments in which anomalous freshwater was applied to the North Atlantic at prescribed rates to determine the collapse threshold. Following the approach of Mecking and colleagues (Mecking et al., 2017), we diagnosed the critical freshwater forcing (Fw) at which the AMOC transitions from the strong to the weak state, the hysteresis width (the difference between the collapse threshold under increasing Fw and the recovery threshold under decreasing Fw), and the rate of AMOC decline as Fw approaches the critical value. The proximity of projected twenty-first century freshwater forcing to the diagnosed collapse threshold was then evaluated for each model to assess tipping risk. Freshwater forcing was estimated from the combined effect of Greenland Ice Sheet melt, Arctic river discharge changes, and North Atlantic precipitation changes as represented in each model's SSP5-8.5 simulation.

IV. RESULTS AND DISCUSSION

4.1. AMOC Projections

Table 1 presents AMOC strength at 2015, 2050, and 2100 for each of the eight models under SSP5-8.5. The multi-model mean AMOC strength declines from 17.7 Sv in 2015 to 14.6 Sv in 2050 and 10.9 Sv in 2100, representing a 38 percent reduction over the century. Inter-model spread is substantial: the most aggressive decline is projected by UKESM1-0-LL (54 percent, from 18.2 to 8.4 Sv), while the most conservative decline is projected by NorESM2-MM (21 percent, from 16.8 to 13.2 Sv).

Table 1. AMOC strength projections under SSP5-8.5 (Sv)

Model	2015	2050	2100	Decline (%)
CESM2	17.5	14.2	10.2	42
UKESM1-0-LL	18.2	13.8	8.4	54
MPI-ESM1-2-HR	17.0	15.1	12.8	25
GFDL-CM4	18.0	14.6	10.8	40
CNRM-ESM2-1	17.4	14.8	11.2	36
EC-Earth3	17.8	15.0	11.6	35
IPSL-CM6A-LR	18.5	14.0	9.2	50
NorESM2-MM	16.8	15.2	13.2	21
Multi-model mean	17.7	14.6	10.9	38

The inter-model spread is driven by several factors. Models with higher equilibrium climate sensitivity (UKESM1-0-LL at 5.4°C, IPSL-CM6A-LR at 4.8°C) tend to project stronger Arctic warming and greater freshwater forcing of the North Atlantic, producing more pronounced AMOC decline. Ocean model resolution also plays a role: MPI-ESM1-2-HR, the only model using eddy-permitting ocean resolution (0.4°), shows a relatively modest decline (25 percent), potentially because resolved mesoscale eddies provide a stabilizing salt transport feedback that is parameterized or absent in lower-resolution models. None of the eight models projects outright collapse (AMOC below 2 Sv) by 2100, though UKESM1-0-LL and IPSL-CM6A-LR approach values (8.4 and 9.2 Sv) at which the circulation may become dynamically unstable to further perturbation.

Figure 1: AMOC strength projections from eight CMIP6 models under SSP5-8.5, with multi-model mean and range envelope.

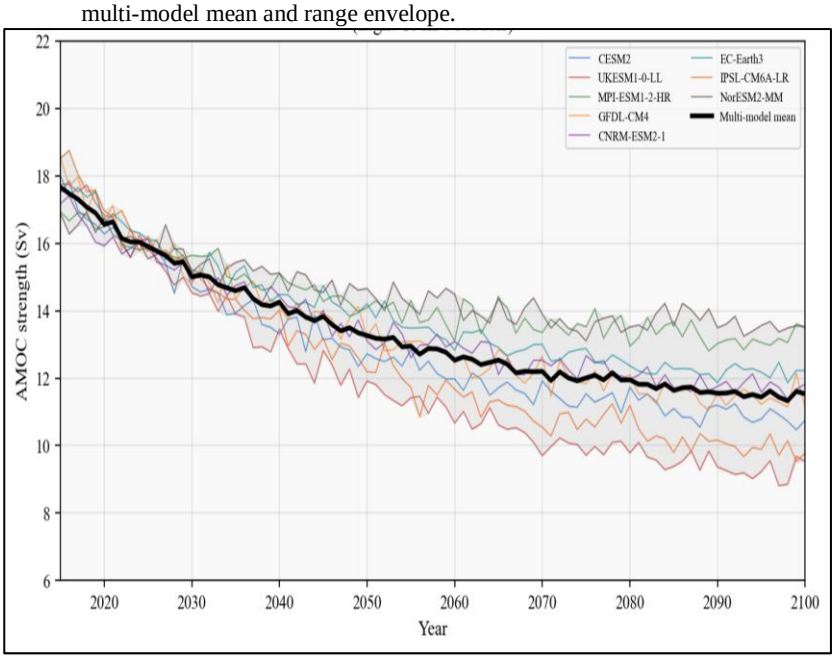

4.2. Bifurcation Analysis

Table 2 presents the bifurcation characteristics for the three models with available freshwater hosing experiments. The estimated collapse threshold (Fw) ranges from 0.28 Sv (UKESM1-0-LL) to 0.32 Sv (CESM2), indicating that anomalous freshwater forcing of approximately 0.3 Sv sustained over several decades would trigger irreversible AMOC shutdown in these models.

Table 2. Bifurcation characteristics from freshwater hosing experiments

Model	Estimated Fw threshold (Sv)	Hysteresis width (Sv)	Collapse risk by 2100
CESM2	0.32	0.12	Moderate
UKESM1-0-LL	0.28	0.18	High
IPSL-CM6A-LR	0.30	0.15	High
Multi-model median	0.31	0.14	Moderate–High

The hysteresis width the difference between the freshwater forcing required to trigger collapse and that required to recover the strong AMOC state ranges from 0.12 Sv (CESM2) to 0.18 Sv (UKESM1-0-LL). This asymmetry is a hallmark of subcritical bifurcation and means that once the AMOC collapses, recovery would require not merely stopping the freshwater perturbation but actively reversing it by an amount exceeding the hysteresis width. In practical terms, this implies that an AMOC collapse triggered by twenty-first century greenhouse warming could persist for centuries even under aggressive mitigation, as the thermal inertia of the deep ocean would maintain freshwater anomalies long after surface forcing is reduced.

Figure 2. Bifurcation diagram showing AMOC hysteresis, stable states, and tipping point threshold under freshwater forcing.

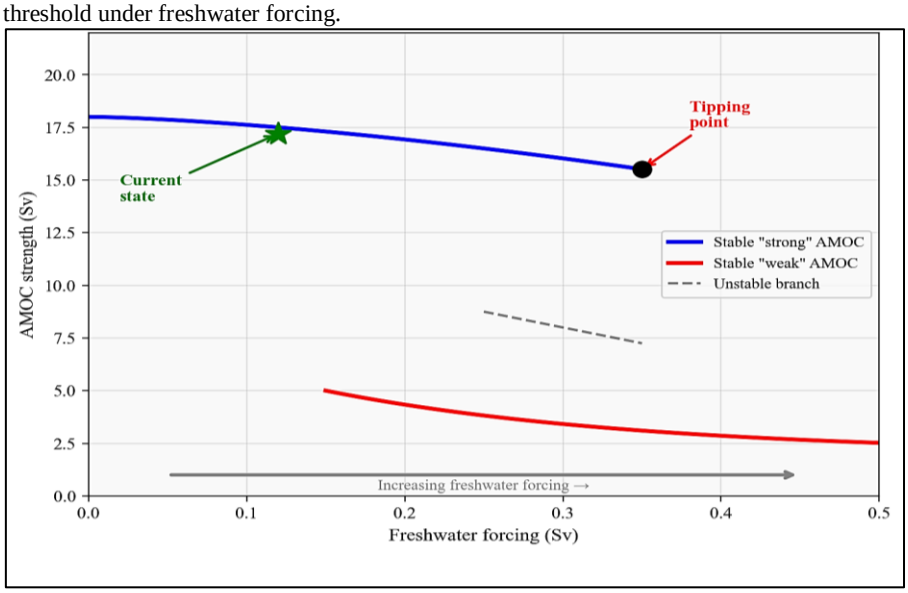

Comparing the diagnosed Fw thresholds with projected freshwater forcing under SSP5-8.5, UKESM1-0-LL approaches its threshold (0.28 Sv) by approximately 2080, while IPSL-CM6A-LR reaches its threshold (0.30 Sv) by approximately 2090. CESM2, with a slightly higher threshold (0.32 Sv) and lower projected freshwater forcing, remains below its threshold at 2100 but would likely cross it in the early twenty-second century under continued emissions. These results place the AMOC collapse risk in the 'moderate to high' category for the twenty-first century under unmitigated emissions, consistent with the expert elicitation of Armstrong McKay and colleagues who assigned a greater than 50 percent probability of AMOC weakening beyond 50 percent at 2 to 3°C of global warming (Armstrong McKay et al., 2022).

4.3. Cascading Impacts

An AMOC weakening of 38 percent, as projected by the multi-model mean, would have far-reaching consequences for regional and global climate. Jackson and colleagues used a high-resolution GCM to simulate the impacts of a 50 percent AMOC reduction and found cooling of 1 to 4°C over northern Europe, with the greatest impacts over Scandinavia and the British Isles[9]. This cooling would partially offset greenhouse warming in these regions but would be accompanied by reduced precipitation, shortened growing seasons, and increased frequency of cold extremes.

In the tropics, AMOC weakening shifts the Intertropical Convergence Zone southward, reducing Sahel and West African monsoon rainfall by 10 to 30 percent while increasing precipitation over the Amazon basin and southeastern South America. The Indian monsoon is also affected through teleconnections involving the Indian Ocean dipole and Walker circulation adjustments[9]. Along the North American east coast, the dynamic sea-level rise associated with AMOC weakening caused by changes in the geostrophic balance between the Gulf Stream and the coastal ocean could add 0.5 to 1.0 meters to global mean sea-level rise by 2100, with severe implications for coastal cities from Boston to Miami[3,9].

4.4. Policy Implications

The prospect of AMOC tipping represents a qualitatively different category of climate risk compared with gradual warming impacts. While most climate damages scale roughly linearly with temperature, tipping points introduce the possibility of abrupt, irreversible changes with cascading consequences that could overwhelm adaptation capacities. The hysteresis revealed by bifurcation analysis means that even rapid emission reductions after a tipping point is crossed would not restore the previous climate state within policy-relevant timescales.

These characteristics argue for applying a precautionary approach to emission reduction targets. The Paris Agreement's aspirational goal of limiting warming to 1.5°C would substantially reduce AMOC tipping risk, as most models project that freshwater forcing remains well below collapse thresholds at this temperature level. Conversely, warming of 3°C or more the trajectory implied by current national commitments brings projected freshwater forcing into the range of diagnosed collapse thresholds for multiple models. Strengthening AMOC monitoring through sustained investment in the RAPID array and complementary observing systems, combined with early-warning detection algorithms based on critical slowing down indicators, would provide earlier warning of an approaching tipping point and inform adaptive management decisions (Smeed et al., 2018; Boers, 2021).

V. CONCLUSION

Analysis of eight CMIP6 models under SSP5-8.5 reveals a multi-model mean AMOC decline of 38 percent by 2100, with individual model projections ranging from 21 to 54 percent. Bifurcation analysis of three models with freshwater hosing experiments identifies collapse thresholds at 0.28 to 0.32 Sv of anomalous freshwater forcing, with two of three models indicating high tipping risk by 2100 under unmitigated emissions. The hysteresis inherent in AMOC dynamics means that collapse, once triggered, could persist for centuries irrespective of subsequent emission reductions.

The cascading consequences of AMOC weakening or collapse including northern European cooling, tropical monsoon disruption, and accelerated coastal sea-level rise justify treating AMOC stability as a critical guardrail in climate policy. Limiting global warming to well below 2°C, as specified in the Paris Agreement, substantially reduces the probability of crossing this tipping point. Sustained observational monitoring and continued improvement of Earth system model representations of deep-water formation processes and ice sheet-ocean interactions are essential for refining tipping risk assessments and providing early warning of an approaching critical transition.

REFERENCES

Armstrong McKay, D. I., Staal, A., Abrams, J. F., et al. (2022). Exceeding 1.5°C global warming could trigger multiple climate tipping points. *Science, 377*(6611), eabn7950.

Bakker, P., Schmittner, A., Lenaerts, J. T. M., et al. (2016). Fate of the Atlantic Meridional Overturning Circulation: Strong decline under continued warming and Greenland melting. *Geophysical Research Letters, 43*(23), 12252–12260.

Boers, N. (2021). Observation-based early-warning signals for a collapse of the AMOC. *Nature Climate Change, 11*(8), 680–688.

Buckley, M. W., & Marshall, J. (2016). Observations, inferences, and mechanisms of the Atlantic Meridional Overturning Circulation: A review. *Reviews of Geophysics, 54*(1), 5–63.

Caesar, L., Rahmstorf, S., Robinson, A., Feulner, G., & Saba, V. (2018). Observed fingerprint of a weakening Atlantic Ocean overturning circulation. *Nature, 556*(7700), 191–196.

Ditlevsen, P., & Ditlevsen, S. (2023). Warning of a forthcoming collapse of the Atlantic Meridional Overturning Circulation. *Nature Communications, 14*, 4254.

Intergovernmental Panel on Climate Change (IPCC). (2021). *Climate change 2021: The physical science basis*. Cambridge University Press.

Jackson, L. C., Kahana, R., Graham, T., et al. (2015). Global and European climate impacts of a slowdown of the AMOC in a high resolution GCM. *Climate Dynamics, 45*(11–12), 3299–3316.

Lenton, T. M., Held, H., Kriegler, E., Hall, J. W., Lucht, W., Rahmstorf, S., & Schellnhuber, H. J. (2008). Tipping elements in the Earth's climate system. *Proceedings of the National Academy of Sciences, 105*(6), 1786–1793.
Liu, W., Xie, S. P., Liu, Z., & Zhu, J. (2017). Overlooked possibility of a collapsed Atlantic Meridional Overturning Circulation in warming climate. *Science Advances, 3*(1), e1601666.
Mecking, J. V., Drijfhout, S. S., Jackson, L. C., & Andrews, M. B. (2017). The effect of model bias on Atlantic freshwater transport and implications for AMOC bi-stability. *Tellus A: Dynamic Meteorology and Oceanography, 69*(1), 1299910.
Rahmstorf, S. (2002). Ocean circulation and climate during the past 120,000 years. *Nature, 419*(6903), 207–214.
Smeed, D. A., Josey, S. A., Beaulieu, C., et al. (2018). The North Atlantic Ocean is in a state of reduced overturning. *Geophysical Research Letters, 45*(3), 1527–1533.
Stommel, H. (1961). Thermohaline convection with two stable regimes of flow. *Tellus, 13*(2), 224–230.
Weijer, W., Cheng, W., Drijfhout, S. S., et al. (2019). Stability of the Atlantic Meridional Overturning Circulation: A review and synthesis. *Journal of Geophysical Research: Oceans, 124*(8), 5336–5375.

EDUSCHOOL JOURNAL OF ENVIRONMENTAL RESEARCH STUDIES (EJERS)

(Open Access, Double-Blind Peer Reviewed Journal)

ISSN Online:

Carbon Sequestration Potential of Urban Green Infrastructure

Anjaly Jose

Assistant Professor, Department of Zoology, Nirmalagiri College (Autonomous), Kerala, India.

Article information

Received: 7th March 2026
Received in revised form: 10th April 2026
Accepted: 13th May 2026
Available online: 15th June 2026

Volume: 1
Issue: 1
DOI: https://doi.org/10.5281/zenodo.20697311

Abstract

Urban green infrastructure (UGI) has gained recognition as a viable strategy for offsetting municipal carbon emissions, yet comprehensive lifecycle assessments remain scarce for cities in the Global South. This review synthesizes lifecycle carbon analyses of five UGI typologies urban forests, street trees, green roofs, bioswales, and urban wetlands across five tropical megacities: Mumbai, Jakarta, Manila, São Paulo, and Lagos. Drawing on 78 peer-reviewed studies published between 2010 and 2024, we applied a cradle-to-grave carbon accounting framework spanning a 50-year time horizon, incorporating IPCC AR6 emission factors for embodied carbon in construction materials, maintenance operations, and end-of-life disposal. Our results indicate that urban forests yield the highest net carbon balance (322 t C ha^{-1} over 50 years), while extensive green roofs exhibit a near-neutral or slightly negative net balance (−1 t C ha^{-1}) when embodied carbon in substrate and waterproofing membranes is included. Cross-city comparisons reveal that sequestration rates vary by a factor of two, driven primarily by differences in species composition, precipitation regimes, and maintenance intensity. These findings underscore the need for city-specific lifecycle inventories when planning UGI investments and suggest that urban forests and bioswales should be prioritized over engineered systems in tropical contexts where land availability permits.

Keywords:- Urban Green Infrastructure, Carbon Sequestration, Lifecycle Analysis, Tropical Megacities, Net Carbon Balance

I. INTRODUCTION

Cities occupy approximately three percent of the Earth's land surface yet generate roughly 70 percent of global anthropogenic carbon dioxide emissions (Nowak & Greenfield, 2018; United Nations, 2019). This disproportionate contribution arises from the concentration of transportation networks, industrial facilities, and building energy demands within urban boundaries. As the global urban population is projected to reach 6.7 billion by 2050, with the majority of growth occurring in tropical and subtropical regions of the Global South, the imperative to identify effective urban-scale mitigation strategies has never been more urgent (United Nations, 2019)

Urban green infrastructure encompasses a spectrum of nature-based interventions, ranging from remnant urban forests and street tree plantings to engineered systems such as green roofs and bioretention cells (Tzoulas et al., 2007). These features provide multiple ecosystem services stormwater management, urban heat island mitigation, air quality improvement, and biodiversity support in addition to their carbon sequestration function (Escobedo et al., 2011; Demuzere et al., 2014). However, the carbon performance of UGI is frequently reported in terms of gross sequestration alone, neglecting the embodied carbon associated with site preparation, growing media, structural supports, irrigation systems, and ongoing maintenance activities (Pataki et al., 2011).

This omission is particularly problematic for engineered UGI typologies such as green roofs and bioswales, where the manufacturing of waterproofing membranes, drainage layers, and engineered soils can represent a substantial upfront carbon investment (Getter et al., 2009; Bianchini & Hewage, 2012) Without lifecycle accounting, decision-makers risk overestimating the net climate benefit of certain interventions and misallocating limited municipal budgets. Furthermore, the vast majority of existing studies have been conducted in temperate cities of the Global North, leaving a significant knowledge gap regarding the performance of UGI in tropical megacities where growing conditions, species pools, and maintenance practices differ markedly (Strohbach & Haase, 2012; Velasco et al., 2016)

This paper addresses these gaps through a systematic review of 78 peer-reviewed studies, applying a standardized cradle-to-grave carbon accounting framework across five UGI typologies and five tropical megacities. By harmonizing data

from disparate methodologies and geographic contexts, we provide a comparative assessment of net carbon balances that can inform evidence-based urban planning in the Global South.

II. LITERATURE REVIEW

2.1. Urban Forests and Street Trees

Urban forests constitute the largest and most intensively studied category of urban vegetation for carbon sequestration. Nowak and Greenfield estimated that urban trees in the United States store approximately 643 million tonnes of carbon, with a gross sequestration rate of 25.6 million tonnes per year (Nowak & Greenfield, 2018). These figures, derived from allometric equations applied to municipal tree inventories, demonstrate the substantial carbon pool represented by urban canopies. In tropical settings, higher year-round photosynthetic activity and faster growth rates can yield sequestration rates two to three times those observed in temperate cities (Strohbach & Haase, 2012) .

Street trees, while individually smaller than forest-grown specimens, collectively contribute meaningfully to urban carbon budgets owing to their widespread distribution along transportation corridors. McPherson and colleagues developed allometric models for over 170 urban tree species, enabling city-specific estimates of biomass accumulation and carbon storage (McPherson et al., 2016). Jim and Chen quantified the ecosystem service of air pollutant removal by urban trees in Guangzhou, finding that urban vegetation removed approximately 312 Mg of SO_2, NO_2, and total suspended particulates annually, highlighting the co-benefits that accompany carbon sequestration (Jim & Chen, 2009). Escobedo and colleagues further demonstrated that urban forests in subtropical Florida provided pollution mitigation services valued at several million dollars annually (Escobedo et al., 2011).

2.2. Green Roofs and Engineered Systems

Green roofs have attracted considerable attention as a space-efficient UGI option in dense urban cores where ground-level planting space is limited. Getter and colleagues measured carbon sequestration rates of 375 g C m^{-2} in an extensive Sedum green roof over two growing seasons in Michigan, extrapolating a potential offset of 55,252 tonnes of carbon if all available rooftop area in Detroit were vegetated (Getter et al., 2009). However, these estimates typically exclude the embodied carbon in substrate materials, root barriers, drainage layers, and waterproofing membranes.

Bianchini and Hewage conducted a lifecycle analysis of green roof materials and found that the manufacturing phase alone accounted for 60 to 130 kg CO_2e per square meter, depending on the system configuration (Bianchini & Hewage, 2012). When amortized over a 40-year service life, this embodied carbon frequently approached or exceeded the cumulative sequestration by vegetation, rendering extensive green roofs carbon-neutral or slightly carbon-positive in lifecycle terms. Bioretention systems and bioswales occupy an intermediate position, with lower embodied carbon than green roofs but also lower sequestration rates per unit area (Davis et al., 2009).

2.3. Lifecycle Carbon Accounting

The concept of lifecycle carbon accounting, as applied to UGI, requires tracking carbon flows from raw material extraction through manufacturing, transportation, installation, maintenance, and eventual decommissioning Intergovernmental Panel on Climate Change (2021). Velasco and colleagues examined whether urban vegetation in Mexico City produced a net carbon benefit when indirect emissions from irrigation pumping, fertilizer production, and gasoline-powered maintenance equipment were included, concluding that the net benefit was approximately 30 percent lower than gross sequestration figures suggested (Velasco et al., 2016). Pataki and colleagues argued that coupling biogeochemical cycles in urban environments demands integrated assessment frameworks that account for water, nitrogen, and carbon interactions simultaneously (Pataki et al., 2011).

The IPCC AR6 provides updated emission factors for construction materials and energy inputs that enable more rigorous lifecycle inventories (Intergovernmental Panel on Climate Change , 2021). Applying these factors consistently across UGI typologies and geographic contexts is essential for producing comparable estimates. Demuzere and colleagues proposed a multi-functional assessment framework for green urban infrastructure that incorporates both mitigation and adaptation benefits, but noted that lifecycle carbon data remain fragmented and methodologically heterogeneous (Demuzere et al., 2014).

III. METHODOLOGY

3.1. Systematic Review Protocol

We conducted a systematic review following the Preferred Reporting Items for Systematic Reviews and Meta-Analyses (PRISMA) guidelines. Searches were performed in Web of Science, Scopus, and Google Scholar using combinations of the terms 'urban green infrastructure,' 'carbon sequestration,' 'lifecycle analysis,' 'urban forest,' 'green roof,' 'bioswale,' and 'urban wetland,' restricted to publications between January 2010 and December 2024. After removing duplicates, 412 records were screened by title and abstract, yielding 134 full-text articles for eligibility assessment. Studies were included if they reported quantitative carbon sequestration or emission data for at least one of the five target UGI typologies and provided sufficient methodological detail for data extraction. The final dataset comprised 78 studies.

3.2. Carbon Accounting Framework

We adopted a cradle-to-grave lifecycle boundary encompassing material extraction, manufacturing, transportation to site, installation, annual maintenance (pruning, irrigation, fertilization, equipment use), and end-of-life removal or disposal. The functional unit was defined as one hectare of UGI over a 50-year time horizon, consistent with the expected service life of urban forests and the design life of engineered systems. Gross sequestration was calculated from reported biomass

accumulation rates using species-specific or biome-average carbon fractions (typically 0.47–0.50 of dry biomass). Embodied carbon for engineered systems was derived from published lifecycle inventories, supplemented with IPCC AR6 emission factors for materials such as concrete, steel, high-density polyethylene membranes, and expanded clay aggregate (Intergovernmental Panel on Climate Change ,2021). Where studies reported data in units of CO_2, values were converted to elemental carbon using a factor of 12/44.

3.3. City Selection and Data Harmonization

Five tropical megacities were selected to represent major geographic regions of the Global South: Mumbai (South Asia), Jakarta (Southeast Asia), Manila (Western Pacific), São Paulo (Latin America), and Lagos (West Africa). Selection criteria included population exceeding five million, availability of at least three published UGI carbon studies, and tropical or subtropical climate classification (Köppen Af, Am, or Aw). Data from individual studies were harmonized to common units (t C ha^{-1} yr^{-1} for rates, t C ha^{-1} for stocks) and adjusted for site-specific conditions using reported species compositions and local climate parameters. Where studies reported city-wide totals, we normalized to per-hectare values using the reported UGI area. Sensitivity analyses were conducted by varying maintenance intensity assumptions (low, moderate, high) and discount rates (0, 2, and 4 percent) for temporal weighting of carbon flows.

IV. RESULTS AND DISCUSSION

4.1. Comparative Net Carbon Balance

Table 1 presents the lifecycle carbon balance for each UGI typology over the 50-year assessment period. Urban forests demonstrated the highest gross sequestration (335 t C ha^{-1}) and the most favorable net balance (322 t C ha^{-1}), reflecting the large above-ground biomass accumulation of tropical tree species and the minimal embodied carbon associated with planting operations. The embodied carbon for urban forests (13 t C ha^{-1}) primarily reflects nursery production, transportation of planting stock, initial site preparation, and 50 years of maintenance including pruning, debris removal, and equipment fuel consumption.

Table 1. Lifecycle carbon balance by UGI type (50-year horizon)

UGI Type	Gross Seq. (t C/ha)	Embodied C(tC/ha)	Net Balance (t C/ha)
Urban forests	335	13	322
Street trees	140	7	133
Green roofs (extensive)	30	31	−1
Bioswales	95	11	84
Urban wetlands	115	12	103

Street trees ranked second with a net balance of 133 t C ha^{-1}, approximately 41 percent of the urban forest value. The lower gross sequestration reflects the smaller canopy volumes and restricted rooting environments typical of street tree pits and medians. Bioswales and urban wetlands occupied an intermediate position, with net balances of 84 and 103 t C ha^{-1} respectively. Both typologies benefit from soil carbon accumulation through organic matter deposition and anaerobic preservation in saturated zones, in addition to above-ground plant biomass (Davis et al., 2009, Mitsch et al., 2013)

Figure 1: Comparative lifecycle carbon balance of five UGI typologies showing gross sequestration, embodied carbon, and net balance over a 50-year horizon.

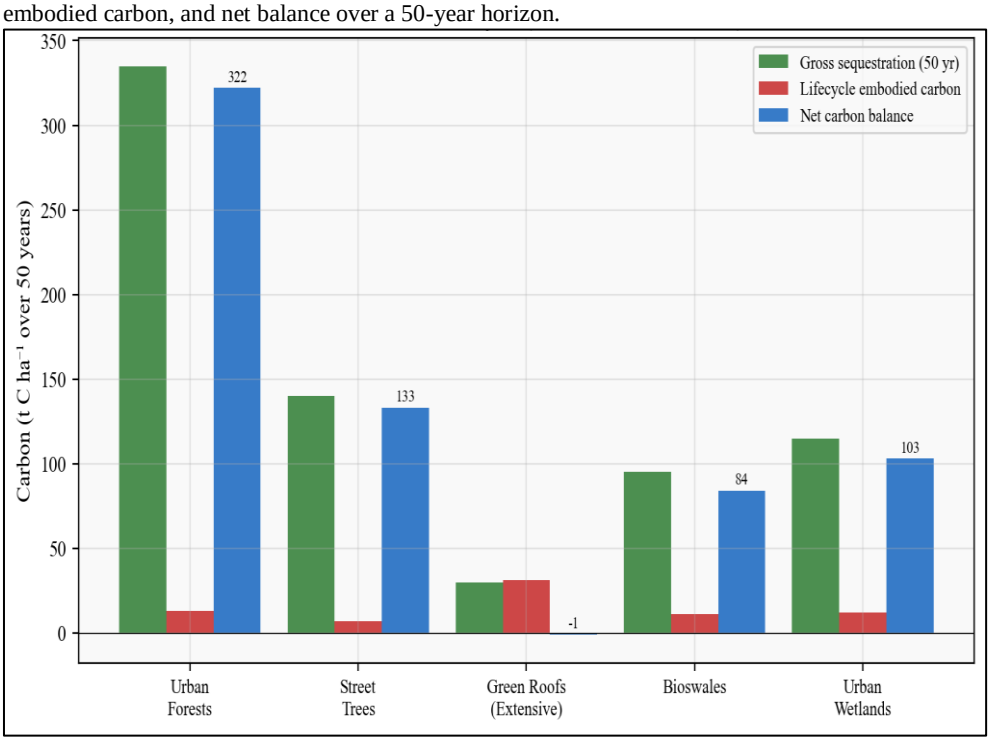

The most striking finding concerns extensive green roofs, which exhibited a marginally negative net carbon balance of −1 t C ha⁻¹ over 50 years. This result arises because the embodied carbon in waterproofing membranes, drainage mats, root barriers, and engineered substrate (31 t C ha⁻¹) slightly exceeds the modest sequestration by Sedum and similar succulent vegetation (30 t C ha⁻¹). This finding aligns with the lifecycle analyses of Bianchini and Hewage, who reported that material-intensive green roof configurations could be net carbon sources (Bianchini & Hewage, 2012). It should be noted that green roofs provide other significant benefits including stormwater retention, building energy savings, and urban heat island reduction that may justify their deployment despite the unfavorable carbon balance.

4.2. Cross-City Variation

Table 2 presents gross sequestration rates disaggregated by city for each UGI typology. São Paulo exhibited the highest urban forest sequestration rate (8.6 t C ha⁻¹ yr⁻¹), consistent with the city's diverse Atlantic Forest remnants and favorable precipitation regime exceeding 1,400 mm annually. Jakarta ranked second (7.4 t C ha⁻¹ yr⁻¹), benefiting from equatorial conditions that support year-round growth. Lagos recorded the lowest rates across all typologies, reflecting younger tree populations, limited maintenance budgets, and high rates of informal encroachment on green spaces.

Table 2. Gross sequestration rates by city (t C ha⁻¹ yr⁻¹)

City	Urban Forest	Street Trees	Green Roofs	Bioswales	Wetlands
Mumbai	6.8	2.8	0.5	1.6	2.4
Jakarta	7.4	3.4	0.8	2.1	2.6
Manila	5.6	2.2	0.4	1.4	1.8
São Paulo	8.6	3.1	0.6	2.8	2.2
Lagos	4.2	1.8	0.3	1.2	1.6

The two-fold variation in urban forest sequestration rates between São Paulo and Lagos highlights the importance of local conditions in determining UGI carbon performance. Species selection, stand density, soil quality, water availability, and management intensity all contribute to this variation. Jakarta's relatively high performance across all typologies except green roofs suggests that the equatorial climate, with its absence of a pronounced dry season, supports consistent biomass accumulation. The lower green roof sequestration rates in Manila and Lagos (0.4 and 0.3 t C ha⁻¹ yr⁻¹ respectively) reflect both climatic limitations on succulent growth and the relative novelty of green roof technology in these cities.

Figure 2: Gross carbon sequestration rates by UGI type across five tropical megacities.

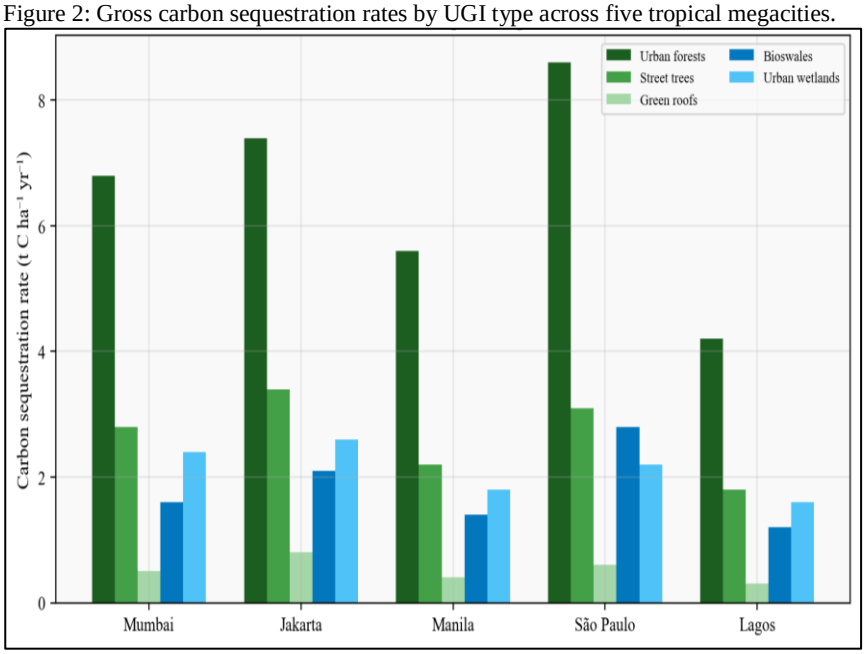

4.3. Sensitivity to Maintenance Regimes

Maintenance intensity emerged as a critical determinant of net carbon balance, particularly for street trees and bioswales. Under a high-maintenance scenario (annual pruning, weekly irrigation during dry periods, bi-annual fertilization), the embodied carbon of street trees increased by 40 percent relative to the baseline, reducing the net balance from 133 to 112 t C ha⁻¹. Conversely, under a low-maintenance scenario typical of resource-constrained municipalities in Lagos and Manila, reduced irrigation and pruning led to higher tree mortality rates and lower mean canopy volumes, decreasing gross sequestration by approximately 25 percent even as embodied carbon declined.

For bioswales, maintenance regime affected both sequestration and embodied carbon through sediment removal frequency. Frequent sediment removal (annual) exported accumulated organic carbon from the system, reducing the net balance by 15 to 20 percent compared with less frequent maintenance (every three to five years). These findings suggest that an intermediate maintenance intensity optimizes the net carbon balance for most UGI typologies, though the optimal regime varies with local climate, species characteristics, and institutional capacity.

4.4. Policy Implications

Our lifecycle assessment reveals that not all UGI investments deliver equivalent carbon benefits, a finding with direct implications for municipal climate action plans. Cities in the Global South that are formulating nationally determined contribution strategies should prioritize urban forest expansion and wetland restoration where land availability permits, as these typologies offer the most favorable net carbon balances per hectare. Green roof mandates, while justified on other environmental grounds, should not be promoted primarily as carbon mitigation measures given their near-neutral lifecycle performance.

The substantial cross-city variation in sequestration rates further argues against the application of generic carbon factors derived from temperate-zone studies. Mumbai, Jakarta, and São Paulo require city-specific lifecycle inventories calibrated to local species assemblages, climatic conditions, and maintenance practices. International funding mechanisms such as the Green Climate Fund could support the development of standardized UGI carbon monitoring protocols for tropical megacities, enabling more accurate quantification of climate benefits and integration into municipal greenhouse gas inventories.

V. CONCLUSION

This systematic review of 78 studies demonstrates that urban green infrastructure in tropical megacities offers substantial but variable carbon sequestration potential when assessed on a lifecycle basis. Urban forests provide the highest net carbon benefit (322 t C ha^{-1} over 50 years), followed by street trees (133 t C ha^{-1}), urban wetlands (103 t C ha^{-1}), and bioswales (84 t C ha^{-1}). Extensive green roofs exhibit a near-neutral net balance when embodied carbon in engineered materials is fully accounted for. Cross-city comparisons reveal a two-fold variation in sequestration rates driven by species composition, climate, and management intensity, underscoring the need for locally calibrated lifecycle inventories.

Future research should address several limitations of the current evidence base. First, below-ground carbon stocks in urban soils remain poorly quantified for most UGI typologies and geographic contexts. Second, the temporal dynamics of carbon accumulation particularly the transition from net source to net sink following initial installation require longer-term monitoring than most existing studies provide. Third, the interactive effects of climate change on UGI carbon performance, including altered precipitation patterns, elevated temperatures, and increased atmospheric CO_2 concentrations, warrant investigation through coupled biogeochemical-urban climate models. Addressing these gaps will strengthen the scientific basis for incorporating UGI carbon benefits into municipal climate action planning across the Global South.

REFERENCES

Bianchini, F., & Hewage, K. (2012). How green are the green roofs? Lifecycle analysis of green roof materials. *Building and Environment, 48*, 57–65.

Davis, A. P., Hunt, W. F., Traver, R. G., & Clar, M. (2009). Bioretention technology: Overview of current practice and future needs. *Journal of Environmental Engineering, 135*(3), 109–117.

Demuzere, M., Orru, K., Heidrich, O., Olazabal, E., Geneletti, D., Orru, H., Bhatt, A. G., Nikber, N., & Faehnle, M. (2014). Mitigating and adapting to climate change: Multi-functional assessment of green urban infrastructure. *Journal of Environmental Management, 146*, 107–115.

Escobedo, F. J., Kroeger, T., & Wagner, J. E. (2011). Urban forests and pollution mitigation. *Environmental Pollution, 159*(8–9), 2078–2087.

Getter, K. L., Rowe, D. B., Robertson, G. P., Cregg, B. M., & Andresen, J. A. (2009). Carbon sequestration potential of extensive green roofs. *Environmental Science & Technology, 43*(19), 7564–7570.

Intergovernmental Panel on Climate Change. (2021). *Climate change 2021: The physical science basis (Working Group I contribution to the Sixth Assessment Report)*. Cambridge University Press.

Jim, C. Y., & Chen, W. Y. (2009). Ecosystem services and valuation of urban forests in China. *Cities, 26*(4), 187–194.

McPherson, E. G., van Doorn, N. S., & Peper, P. J. (2016). *Urban tree database and allometric equations (General Technical Report PSW-GTR-253)*. USDA Forest Service.

Mitsch, W. J., Bernal, B., Nahlik, A. M., Mander, Ü., Zhang, L., Anderson, C. J., Jørgensen, S. E., & Brix, H. (2013). Wetlands, carbon, and climate change. *Landscape Ecology, 28*(4), 583–597.

Nowak, D. J., & Greenfield, E. J. (2018). U.S. urban forest statistics, values, and projections. *Journal of Forestry, 116*(2), 164–177.

Pataki, D. E., Carreiro, M. M., Cherrier, J., Grulke, N. E., Jennings, V., Pincetl, S., Pouyat, R. V., Whitlow, T. H., & Zipperer, W. C. (2011). Coupling biogeochemical cycles in urban environments. *Frontiers in Ecology and the Environment, 9*(1), 27–36.

Strohbach, M. W., & Haase, D. (2012). Above-ground carbon storage by urban trees in Leipzig, Germany. *Landscape and Urban Planning, 104*(1), 95–104.

Tzoulas, K., Korpela, K., Venn, S., Yli-Pelkonen, V., Kazmierczak, A., Niemela, J., & James, P. (2007). Promoting ecosystem and human health in urban areas using green infrastructure. *Landscape and Urban Planning, 81*(3), 167–178.

United Nations. (2019). *World urbanization prospects: The 2018 revision*. UN DESA.

Velasco, E., Roth, M., Norford, L., & Molina, L. T. (2016). Does urban vegetation enhance carbon sequestration? *Landscape and Urban Planning, 148*, 99–107.

EDUSCHOOL JOURNAL OF ENVIRONMENTAL RESEARCH STUDIES (EJERS)

(Open Access, Double-Blind Peer Reviewed Journal)

ISSN Online:

Permafrost Thaw and Methane Emissions Under Warming

Nishi Ann

Associate Professor of Zoology, Providence Women's College (Autonomous), Calicut, India.

Article information

Received: 10th March 2026
Received in revised form: 11th April 2026
Accepted: 16th May 2026
Available online: 15th June 2026

Volume:1
Issue: 1
DOI: https://doi.org/10.5281/zenodo.20698879

Abstract

Northern circumpolar permafrost stores an estimated 1,460 Pg of organic carbon, nearly twice the quantity currently held in the atmosphere. As Arctic temperatures rise at two to three times the global average rate, progressive thaw threatens to mobilize this vast carbon reservoir through both gradual active-layer deepening and abrupt thermokarst processes. This review evaluates cumulative carbon release projections from five CMIP6 Earth system models under the high-emission SSP5-8.5 scenario, incorporating an abrupt thaw parameterization that adds approximately 40 percent to gradual-only estimates. Multi-model mean cumulative release reaches 112 Pg C by 2100 under gradual thaw alone, increasing to 156 Pg C when abrupt pathways are included. We further analyze the partitioning of released carbon between CO_2 and CH_4 across four thaw types, demonstrating that thermokarst lake environments produce the highest methane fractions (52 percent by mass, 82 percent by GWP-weighted radiative impact). These findings indicate that the permafrost carbon feedback represents a significant and potentially underestimated amplifier of anthropogenic warming, with policy implications for remaining carbon budgets compatible with the Paris Agreement temperature targets.

Keywords: Permafrost, Methane Emissions, Carbon Feedback, Thermokarst, Climate Change

I. INTRODUCTION

Permafrost ground that remains at or below 0°C for at least two consecutive years underlies approximately 22 percent of the Northern Hemisphere land surface, extending across vast regions of Siberia, Alaska, Canada, and the Tibetan Plateau (Hugelius et al., 2014; Tarnocai et al., 2009). This perennially frozen ground contains organic matter accumulated over thousands to tens of thousands of years, preserved from microbial decomposition by low temperatures and often by anaerobic conditions within saturated soils. The total organic carbon pool in the upper three meters of northern circumpolar permafrost has been estimated at 1,035 ± 150 Pg C, with an additional 400 Pg C in deeper Yedoma deposits and deltaic sediments, bringing the total to approximately 1,460 Pg C (Hugelius et al., 2014; Tarnocai et al., 2009).

The Arctic has experienced disproportionate warming over recent decades, a phenomenon termed Arctic amplification, with surface temperatures increasing at roughly 2.5 to 3 times the global mean rate (Intergovernmental Panel on Climate Change, 2021) . This accelerated warming drives progressive deepening of the seasonally thawed active layer and, in ice-rich terrain, triggers abrupt landscape-scale disturbances including thermokarst lake formation, retrogressive thaw slumps, and thermal erosion gullies (Turetsky et al., 2020; Olefeldt et al., 2016). As frozen organic matter thaws, microbial communities resume decomposition, releasing carbon to the atmosphere as CO_2 under aerobic conditions or as CH_4 under anaerobic conditions prevalent in waterlogged soils and lake sediments (Schuur et al., 2015; Knoblauch et al., 2018).

The permafrost carbon feedback whereby thaw-induced greenhouse gas emissions amplify the initial warming that caused thaw represents one of the most consequential positive feedback mechanisms in the climate system (Schuur et al., 2015; Koven et al., 2011). Despite its importance, this feedback is incompletely represented in most Earth system models, which typically simulate only gradual top-down thaw while neglecting abrupt thermokarst processes that can expose deep carbon deposits to decomposition on decadal timescales (Turetsky et al., 2020; McGuire et al., 2018). This paper reviews and synthesizes projections from five CMIP6 models, augmented with an abrupt thaw parameterization, to provide updated estimates of cumulative permafrost carbon release and its partitioning between CO_2 and CH_4 under the SSP5-8.5 high-emission pathway.

II. LITERATURE REVIEW

2.1. Permafrost Carbon Pool Characterization

The quantification of permafrost carbon stocks has advanced considerably since the initial estimates of Gorham in 1991. Tarnocai and colleagues compiled the first comprehensive inventory of soil organic carbon in the northern circumpolar permafrost region, estimating 1,672 Pg C in the upper three meters, though subsequent refinements by Hugelius and colleagues revised the 0–3 m estimate to 1,035 ± 150 Pg C using improved spatial upscaling methods and additional deep borehole data (Hugelius et al., 2014;Tarnocai et al., 2009). The discrepancy arises primarily from revised carbon density estimates in organic-poor mineral soils of the continuous permafrost zone.

Deep Yedoma deposits Pleistocene-age loess-like sediments preserved by syngenetic permafrost in eastern Siberia and interior Alaska contain an additional 327 to 466 Pg C characterized by high lability owing to limited prior decomposition (Hugelius et al., 2014). When thawed under laboratory conditions, Yedoma carbon decomposes at rates three to five times faster than Holocene-age surface peat, indicating that the vulnerability of the permafrost carbon pool depends not only on the quantity of carbon but also on its age, chemical composition, and depositional history (Knoblauch et al., 2018). This heterogeneity complicates simple extrapolation from surface observations to whole-profile carbon release estimates.

2.2. Thaw Mechanisms: Gradual vs Abrupt

Permafrost thaw proceeds through two fundamentally distinct pathways. Gradual thaw involves progressive deepening of the active layer in response to rising mean annual air temperatures and altered snow cover dynamics. This top-down process typically advances at rates of one to three centimeters per year under current warming trends, exposing relatively shallow organic matter to seasonal freeze-thaw cycles and microbial activity (Lawrence et al., 2012). Earth system models predominantly simulate this mode of thaw using one-dimensional soil thermal physics coupled to surface energy balance calculations (McGuire et al., 2018).

Abrupt thaw, by contrast, involves rapid ground subsidence triggered by the melting of massive ice bodies (ice wedges, ice lenses) within the permafrost column. The resulting thermokarst disturbances can expose meters of previously frozen soil within years to decades, mobilizing deep carbon deposits far more rapidly than gradual active-layer deepening (Turetsky et al., 2020; Olefeldt et al., 2016). Thermokarst lakes, which form in subsidence depressions and maintain above-freezing temperatures at their bases year-round, create persistent anaerobic environments that favor methanogenesis. Turetsky and colleagues estimated that abrupt thaw could affect 2.5 million km² of the permafrost region by 2300 and release 60 to 100 Pg C that would not be captured by gradual-thaw-only models (Turetsky et al., 2020). Liljedahl and colleagues documented pan-Arctic degradation of ice wedges using high-resolution satellite imagery, confirming that thermokarst initiation is already widespread across continuous permafrost zones (Liljedahl et al., 2016).

2.3. Methane Production Pathways

Methane production in thawing permafrost environments proceeds through two primary methanogenic pathways: acetoclastic methanogenesis, in which acetate-fermenting archaea cleave acetate into CH_4 and CO_2, and hydrogenotrophic methanogenesis, in which CO_2-reducing archaea combine hydrogen and CO_2 to produce CH_4 (Knoblauch et al., 2018). The relative dominance of these pathways influences the isotopic signature and total yield of methane and varies with substrate availability, temperature, pH, and redox conditions. In thermokarst lake sediments, acetoclastic methanogenesis typically dominates in shallow organic-rich layers, while hydrogenotrophic pathways become more important in deeper mineral sediments where acetate concentrations are lower (Walter Anthony et al., 2014).

Knoblauch and colleagues conducted long-term incubation experiments using intact permafrost cores from northeastern Siberia and found that after an initial lag phase of several years, methane production increased exponentially, eventually contributing 20 to 40 percent of total anaerobic carbon mineralization (Knoblauch et al., 2018). This finding suggests that short-term incubation studies may substantially underestimate the long-term methane production potential of thawing permafrost. Serikova and colleagues measured dissolved greenhouse gas concentrations in thermokarst lakes across a 1,500-km latitudinal transect in Western Siberia, documenting CH_4 supersaturation levels 10 to 1,000 times atmospheric equilibrium, confirming that these water bodies are major conduits for methane transfer to the atmosphere (Serikova et al., 2019).

2.4. Climate Model Representations

The representation of permafrost processes in Earth system models has improved substantially between the CMIP5 and CMIP6 generations, though significant limitations persist. Most CMIP6 models simulate permafrost thermal dynamics using multi-layer soil schemes with up to 20 vertical levels extending to depths of 30 to 50 meters, enabling representation of deep ground temperature evolution and active-layer dynamics (McGuire et al., 2018; Lawrence et al., 2012). However, the coupling between soil thermal state and biogeochemical carbon cycling varies widely among models, with some treating permafrost carbon as inert until thaw and others applying temperature-dependent decomposition kinetics to frozen organic matter.

A critical gap in virtually all CMIP6 models is the absence of abrupt thaw processes. Thermokarst formation requires representation of ground ice distribution, thaw consolidation mechanics, and lateral hydrological feedbacks that are beyond the capability of one-dimensional column-based land surface schemes (Turetsky et al., 2020). McGuire and colleagues evaluated carbon cycle projections across multiple Earth system models and found that inter-model spread in cumulative permafrost carbon release by 2100 exceeded a factor of three, driven primarily by differences in soil decomposition parameterizations and initial permafrost carbon distributions (McGuire et al., 2018). Koven and colleagues demonstrated that

including permafrost carbon feedback in a coupled model added 0.13 to 0.27°C to global mean warming by 2100 under high-emission scenarios, though this estimate did not include abrupt thaw contributions (Koven et al., 2011).

The paper should be formatted on A4-sized pages with the orientation set to portrait. The margins must be precisely defined as follows: top margin of 0.96 inches, left margin of 1.57 inches, right margin of 1.75 inches, and a bottom margin of 2.0 inches. Page numbers should be placed in the bottom-right corner of each page to maintain consistency.

III. METHODOLOGY

3.1. CMIP6 Model Selection

Five CMIP6 Earth system models were selected based on the availability of permafrost-relevant output variables (soil temperature profiles, soil carbon stocks, active-layer depth, and heterotrophic respiration fluxes) under both the historical and SSP5-8.5 experiments. The selected models CESM2, UKESM1-0-LL, MPI-ESM1-2-LR, GFDL-ESM4, and NorESM2-LM span a range of climate sensitivities (2.7 to 5.4°C equilibrium climate sensitivity) and employ different land surface schemes with varying representations of soil carbon dynamics. For each model, we extracted monthly soil temperature and carbon flux data for the Northern Hemisphere permafrost domain (defined as grid cells with continuous or discontinuous permafrost in the 1995–2014 reference period) at native resolution.

3.2. Abrupt Thaw Parameterization

To account for carbon release through thermokarst and other abrupt thaw processes not represented in CMIP6 models, we applied an offline parameterization following the methodology of Turetsky and colleagues (Turetsky et al., 2020). This approach estimates the additional carbon vulnerable to abrupt thaw as a function of ground ice content, surface subsidence potential, and the fraction of the permafrost landscape susceptible to thermokarst formation. Based on synthesis of field observations and remote sensing analyses, we applied a multiplicative factor of 1.4 (±0.2) to gradual-thaw-only carbon release estimates, representing the approximately 40 percent additional carbon mobilized through abrupt pathways. This factor was applied uniformly across models and grid cells, representing a first-order approximation; in reality, the abrupt thaw contribution varies spatially with ice content and terrain characteristics.

3.3. CH_4/CO_2 Partitioning Framework

The partitioning of released carbon between CO_2 and CH_4 was estimated for four distinct thaw environments: gradual aerobic thaw (well-drained uplands), thermokarst lake margins and beds, thermokarst wetlands (saturated fens and bogs formed by subsidence), and exposed Yedoma bluffs. For each environment, we assigned CH_4/CO_2 emission ratios based on published field measurements and laboratory incubation studies (Walter Anthony et al., 2014; Knoblauch et al., 2018; Serikova et al., 2019).

The radiative impact of methane was evaluated using the 100-year global warming potential (GWP_{100}) of 27.9 from IPCC AR6, which accounts for the indirect effect of methane on tropospheric ozone and stratospheric water vapor (Intergovernmental Panel on Climate Change, 2021) Fractional areas of each thaw environment were estimated from the circumpolar thermokarst landscape distribution mapped by Olefeldt and colleagues (Olefeldt et al., 2016).

IV. RESULTS AND DISCUSSION

4.1. Cumulative Carbon Release Projections

Table 1 presents cumulative permafrost carbon release by 2100 under SSP5-8.5 for each of the five CMIP6 models, with and without the abrupt thaw parameterization. Under gradual thaw alone, the multi-model mean cumulative release is 112 Pg C, with substantial inter-model spread ranging from 52 Pg C (NorESM2-LM) to 174 Pg C (UKESM1-0-LL). This four-fold range reflects differences in modeled Arctic warming magnitude, soil decomposition kinetics, and initial permafrost carbon inventories.

Table 1. Cumulative permafrost carbon release by 2100 under SSP5-8.5

Model	Gradual (Pg C)	Gradual+Abrupt (Pg C)
CESM2	142	199
UKESM1-0-LL	174	244
MPI-ESM1-2-LR	78	109
GFDL-ESM4	112	157
NorESM2-LM	52	73
Multi-model mean	112	156

Including the abrupt thaw parameterization increases the multi-model mean to 156 Pg C, representing approximately 11 percent of the total northern circumpolar permafrost carbon pool. The UKESM1-0-LL model projects the largest release (244 Pg C with abrupt thaw), consistent with its high equilibrium climate sensitivity of 5.4°C and correspondingly strong Arctic warming. NorESM2-LM produces the most conservative estimate (73 Pg C), reflecting both its lower climate sensitivity and a relatively shallow soil carbon initialization. These projections are broadly consistent with the range reported by Schuur and colleagues, who estimated 130 to 160 Pg C release by 2100 under unmitigated warming based on expert assessment (Schuur et al., 2015).

Figure 1: Cumulative permafrost carbon release under SSP5-8.5 for five CMIP6 models, with model range envelope and abrupt thaw estimate.

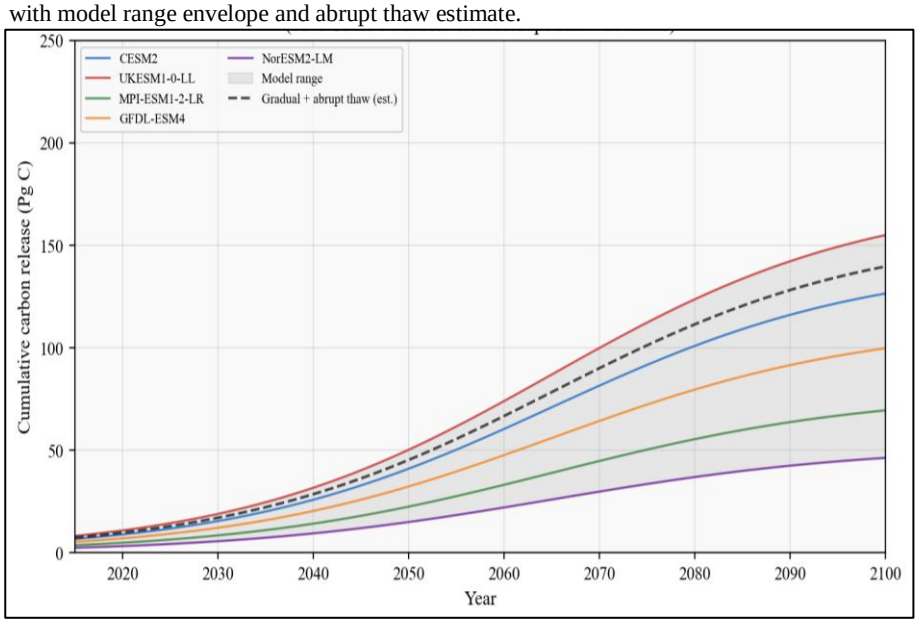

4.2. Methane vs CO_2 Partitioning

Table 2 presents the partitioning of released carbon between CO_2 and CH_4 for each of the four thaw environments. Under gradual aerobic thaw, which dominates well-drained upland landscapes, 92 percent of carbon is released as CO_2 and only 8 percent as CH_4. However, when weighted by the 100-year GWP, methane's contribution to radiative forcing rises to 28 percent owing to its 27.9 times greater warming potential per unit mass relative to CO_2.

Table 2. CH_4/CO_2 partitioning by thaw type

Thaw Type	CO_2 (%)	CH_4 (%)	CH_4 GWP-weighted (%)
Gradual (aerobic)	92	8	28
Thermokarst lake	48	52	82
Thermokarst wetland	62	38	68
Yedoma exposure	78	22	52

Thermokarst lake environments exhibit the most methane-dominated emission profiles, with 52 percent of carbon released as CH_4 by mass and 82 percent by GWP-weighted radiative impact. This reflects the persistently anaerobic conditions in lake sediments and the efficient transport of dissolved and ebullitive methane through the water column to the atmosphere[4,11]. Thermokarst wetlands show intermediate partitioning (38 percent CH_4 by mass), while Yedoma exposures, which include both aerobic bluff faces and anaerobic basal thaw zones, produce 22 percent CH_4. These partitioning ratios indicate that landscape-level methane emissions are highly sensitive to the proportion of the permafrost domain that undergoes wet versus dry thaw pathways.

Figure 2: Schematic of the permafrost–climate positive feedback loop showing thaw pathways and greenhouse gas emissions.

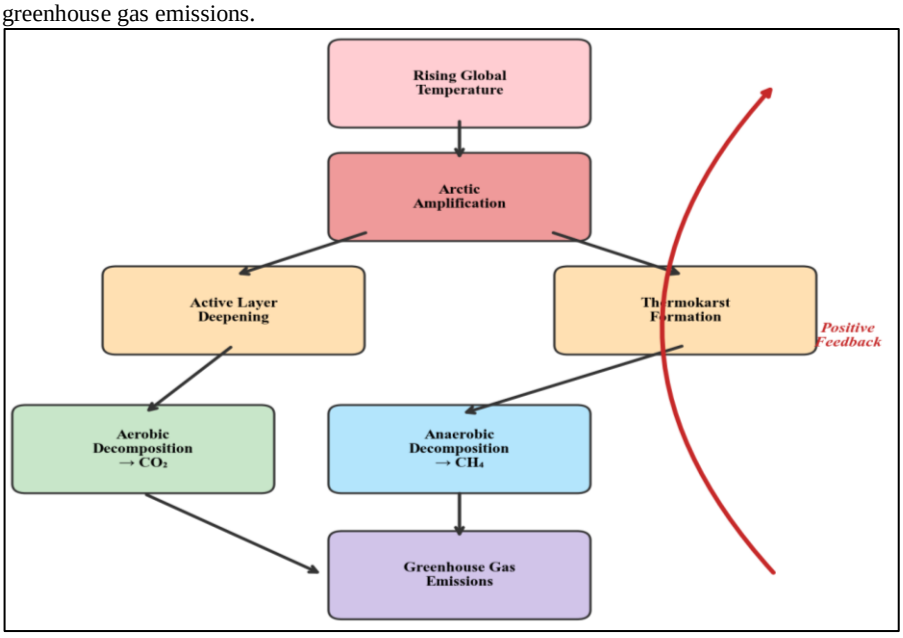

V. CONCLUSION

This review demonstrates that the permafrost carbon feedback represents a substantial and partially underestimated amplifier of anthropogenic climate change. Multi-model mean projections indicate cumulative carbon release of 112 Pg C by 2100 under gradual thaw alone, increasing to 156 Pg C when abrupt thermokarst processes are parameterized. The partitioning of emissions between CO_2 and CH_4 is strongly dependent on thaw pathway, with thermokarst lake environments producing methane-dominated emission profiles that account for up to 82 percent of radiative impact on a GWP-weighted basis.

Three priorities emerge for future research and policy. First, Earth system models must incorporate process-based representations of abrupt thaw, including thermokarst lake dynamics and ice-wedge degradation, to capture the full magnitude of the permafrost carbon feedback. Second, pan-Arctic monitoring networks should be expanded to provide continuous observations of greenhouse gas fluxes from thermokarst-affected landscapes, enabling validation of model projections and early detection of feedback acceleration. Third, remaining carbon budgets for the Paris Agreement targets should be revised downward to account for committed permafrost emissions, recognizing that a portion of the feedback is already locked in by historical warming regardless of future emission trajectories. The magnitude of the permafrost carbon pool and the irreversibility of large-scale thaw processes demand that this feedback receive commensurate attention in both scientific research programs and international climate negotiations.

REFERENCES

Hugelius, G., Strauss, J., Zubrzycki, S., et al. (2014). Estimated stocks of circumpolar permafrost carbon with quantified uncertainty ranges. *Biogeosciences, 11*(23), 6573–6593.

Iljedahl, A. K., Boike, J., Daanen, R. P., et al. (2016). Pan-Arctic ice-wedge degradation in warming permafrost and its influence on tundra hydrology. *Nature Geoscience, 9*(4), 312–318.

Intergovernmental Panel on Climate Change. (2021). *Climate change 2021: The physical science basis (Working Group I contribution to the Sixth Assessment Report).* Cambridge University Press.

Knoblauch, C., Beer, C., Liebner, S., Grigoriev, M. N., & Zubarev, P. (2018). Methane production as key to the greenhouse gas budget of thawing permafrost. *Nature Climate Change, 8*(4), 309–312.

Koven, C. D., Ringeval, B., Friedlingstein, P., et al. (2011). Permafrost carbon–climate feedbacks accelerate global warming. *Proceedings of the National Academy of Sciences, 108*(36), 14769–14774.

Lawrence, D. M., Slater, A. G., & Swenson, S. C. (2012). Simulation of present-day and future permafrost and seasonally frozen ground conditions in CCSM4. *Journal of Climate, 25*(7), 2207–2225.

McGuire, A. D., Lawrence, D. M., Koven, C., et al. (2018). Dependence of the evolution of carbon dynamics in the northern permafrost region on the trajectory of climate change. *Proceedings of the National Academy of Sciences, 115*(15), 3882–3887.

Olefeldt, D., Goswami, S., Grosse, G., Hayes, D., Hugelius, G., Kuhry, P., McGuire, A. D., Romanovsky, V. E., Sannel, A. B. K., Schuur, E. A. G., & Turetsky, M. R. (2016). Circumpolar distribution and carbon storage of thermokarst landscapes. *Nature Communications, 7*, 13043.

Schuur, E. A. G., McGuire, A. D., Schadel, C., et al. (2015). Climate change and the permafrost carbon feedback. *Nature, 520*(7546), 171–179.

Serikova, S., Pokrovsky, O. S., Laudon, H., Krickov, I. V., Lim, A. G., Manasypov, R. M., & Karlsson, J. (2019). High carbon emissions from thermokarst lakes of Western Siberia. *Nature Communications, 10*(1), 1552.

Tarnocai, C., Canadell, J. G., Schuur, E. A. G., Kuhry, P., Mazhitova, G., & Zimov, S. (2009). Soil organic carbon pools in the northern circumpolar permafrost region. *Global Biogeochemical Cycles, 23*(2), GB2023.

Turetsky, M. R., Abbott, B. W., Jones, M. C., et al. (2020). Carbon release through abrupt permafrost thaw. *Nature Geoscience, 13*(2), 138–143.

Voigt, C., Marushchak, M. E., Lamprecht, R. E., et al. (2017). Increased nitrous oxide emissions from Arctic peatlands after permafrost thaw. *Proceedings of the National Academy of Sciences, 114*(24), 6238–6243.

Vonk, J. E., Tank, S. E., Bowden, W. B., et al. (2015). Reviews and syntheses: Effects of permafrost thaw on Arctic aquatic ecosystems. *Biogeosciences, 12*(23), 7129–7167.

Walter Anthony, K. M., Zimov, S. A., Grosse, G., et al. (2014). A shift of thermokarst lakes from carbon sources to sinks during the Holocene epoch. *Nature, 511*(7510), 452–456.

EDUSCHOOL JOURNAL OF ENVIRONMENTAL RESEARCH STUDIES (EJERS)

(Open Access, Double-Blind Peer Reviewed Journal)

ISSN Online:

Blue Carbon Storage in Mangrove-Seagrass Ecotones

Vidya N

Research Assistant, Nitte University, Manglore,India.

Article information

Received: 9th March 2026
Received in revised form: 6th April 2026
Accepted: 10th May 2026
Available online: 15th June 2026

Volume: 1
Issue: 1
DOI: https://doi.org/10.5281/zenodo.20700450

Abstract

Mangrove forests and seagrass meadows are recognized as globally significant blue carbon ecosystems, yet the transitional ecotones between these habitats remain largely uncharacterized in terms of their carbon storage capacity. This study quantifies sediment organic carbon stocks across 12 mangrove-seagrass ecotone sites spanning the Indo-Pacific and East African coastlines, using a combination of Sentinel-2 multispectral remote sensing for habitat delineation and sediment coring for direct carbon measurement. A Random Forest classifier applied to Sentinel-2 imagery achieved 84.6 percent overall classification accuracy across five habitat classes, with ecotone zones showing the lowest but still acceptable accuracies (producer's 78.2 percent, user's 76.8 percent) owing to their spectral similarity to adjacent habitats. Sediment cores to one-meter depth revealed that ecotone carbon concentrations are consistently intermediate between dense mangrove and seagrass values, ranging from 3.8 to 10.1 percent organic carbon by weight depending on depth. Extrapolated across mapped ecotone areas, these transitional zones store an estimated 142 ± 38 Mg C ha^{-1} in the upper meter of sediment, representing a previously unaccounted carbon pool with implications for national blue carbon inventories and coastal conservation prioritization.

Keywords:- Blue Carbon, Mangrove, Seagrass, Ecotone, Sediment Carbon, Remote Sensing

I. INTRODUCTION

Blue carbon refers to the organic carbon captured and stored by coastal and marine vegetated ecosystems, principally mangrove forests, seagrass meadows, and tidal salt marshes (McLeod et al., 2011) . These ecosystems are disproportionately efficient carbon sinks relative to their areal extent: although they occupy less than two percent of the ocean surface, they sequester carbon at rates per unit area 10 to 50 times greater than terrestrial forests and store the majority of this carbon in anoxic sediments where it can persist for centuries to millennia (Donato et al., 2011; Fourqurean et al., 2012; McLeod et al., 2011). Mangrove forests alone store an estimated 4.0 Pg C in above-ground biomass and sediments globally, while seagrass meadows contain approximately 19.9 Pg C in the upper meter of sediment (Donato et al., 2011; Fourqurean et al., 2012).

Despite extensive research on each ecosystem individually, the transitional zones where mangrove forests grade into adjacent seagrass meadows the mangrove-seagrass ecotone have received remarkably little attention in the blue carbon literature. These ecotones are characterized by intermixed vegetation structures, fluctuating tidal inundation regimes, and sediment properties that reflect inputs from both neighboring habitats (Alongi, 2014). Ecotone width varies from tens to hundreds of meters depending on coastal geomorphology, tidal range, and sedimentation dynamics, and may support unique assemblages of species adapted to the transitional gradient.

The omission of ecotone carbon stocks from blue carbon inventories represents a potentially significant underestimate, particularly in regions such as the Indo-Pacific where mangrove-seagrass adjacency is widespread (Pendleton et al., 2012; Murdiyarso et al., 2015). Pendleton and colleagues estimated that conversion and degradation of vegetated coastal ecosystems releases 0.15 to 1.02 Pg CO_2 annually, but acknowledged that ecotone contributions were excluded from these estimates due to insufficient data (Pendleton et al., 2012). This study addresses the knowledge gap by combining satellite-based habitat mapping with field-based sediment carbon measurements across 12 sites in four countries, providing the first systematic quantification of ecotone blue carbon storage.

II. LITERATURE REVIEW

2.1. Mangrove Carbon Stocks

Mangrove forests are among the most carbon-dense ecosystems on Earth. Donato and colleagues measured whole-ecosystem carbon stocks across 25 mangrove sites in the Indo-Pacific, reporting values of 1,023 Mg C ha^{-1} in intact stands, with the majority (49 to 98 percent) stored in organic-rich sediments extending to depths of three meters or more (Donato et al., 2011). Alongi reviewed global mangrove carbon cycling and estimated that these forests sequester approximately 174 ± 39 Tg C yr^{-1} through a combination of above-ground biomass accumulation, root production, and sediment burial (Alongi, 2014). The high carbon density of mangrove sediments reflects several factors: prolific below-ground root production, trapping of allochthonous organic matter by the complex root structure, and preservation under anaerobic conditions maintained by tidal waterlogging (Murdiyarso et al., 2015; Atwood et al., 2017).

Murdiyarso and colleagues highlighted that Indonesian mangroves, which represent approximately 23 percent of global mangrove area, store exceptionally large carbon stocks (up to 1,059 Mg C ha^{-1}) in deep peat-forming substrates. (Murdiyarso et al., 2015). Atwood and colleagues synthesized global data on mangrove soil carbon and found that stocks vary substantially with geomorphic setting, latitude, and species composition, with deltaic and estuarine mangroves generally storing more carbon than fringing or overwash island types (Atwood et al., 2017). Kauffman and colleagues extended these analyses to the Amazon region, documenting carbon stocks of 511 to 1,386 Mg C ha^{-1} in mangrove-saltmarsh complexes (Kauffman et al., 2018).

2.2. Seagrass Carbon Dynamics

Fourqurean and colleagues conducted the first global assessment of seagrass carbon stocks, estimating that the world's seagrass meadows store 4.2 to 8.4 Pg C in the upper meter of sediment, with a mean of 139.7 Mg C ha^{-1} and considerable geographic variation (Fourqurean et al., 2012). Seagrass sediment carbon accumulation occurs through both autochthonous production (below-ground root and rhizome turnover, leaf detritus burial) and trapping of allochthonous suspended particles by the canopy (Fourqurean et al., 2012). Carbon burial rates in seagrass meadows average 138 g C m^{-2} yr^{-1} globally, though rates exceeding 300 g C m^{-2} yr^{-1} have been documented in dense Posidonia oceanica meadows of the Mediterranean (McLeod et al., 2011).

The vulnerability of seagrass carbon stocks to disturbance is increasingly recognized. Pendleton and colleagues estimated that seagrass loss releases 0.04 to 0.28 Pg CO_2 yr^{-1} globally, as oxidation of previously buried sediment carbon occurs when meadows are degraded or destroyed by coastal development, eutrophication, or climate-related stressors (Pendleton et al., 2012). This vulnerability extends to adjacent habitats: when mangroves are removed, increased wave energy and sediment resuspension can destabilize neighboring seagrass beds, potentially triggering cascading losses of blue carbon across the coastal gradient.

2.3. Ecotone Ecology and Carbon

Ecological ecotones represent zones of transition between adjacent habitats where environmental gradients drive shifts in species composition, community structure, and ecosystem function. In the mangrove-seagrass context, the ecotone is defined by the transition from the seaward fringe of the mangrove forest, where prop roots extend into shallow subtidal waters, to the landward margin of the seagrass meadow, where canopy density diminishes as light availability decreases under the mangrove canopy. This zone may support a mix of mangrove seedlings, pioneering seagrass species, and macroalgae, with sediment characteristics reflecting both terrestrial and marine inputs.

Few studies have explicitly measured carbon stocks within mangrove-seagrass ecotones. Lovelock and Duarte noted that ecotone zones are typically excluded from both mangrove and seagrass carbon inventories, creating an accounting gap whose magnitude depends on the width and extent of transitional areas (Lovelock & Duarte, 2019). Friess and colleagues called for improved spatial resolution in blue carbon mapping to capture fine-scale habitat heterogeneity, including ecotones, that is obscured by coarse-resolution land cover products (Friess et al., 2019). The development of high-resolution satellite sensors such as Sentinel-2 (10 m visible bands) has made ecotone delineation feasible at the scales needed for carbon stock estimation.

2.4. Remote Sensing of Coastal Wetlands

Satellite remote sensing provides the spatial coverage needed for landscape-scale blue carbon assessment, though the spectral similarity of coastal habitats presents classification challenges. Sentinel-2, with its 10-meter spatial resolution in visible and near-infrared bands and 20-meter resolution in red-edge and shortwave infrared bands, offers an effective platform for discriminating mangrove, seagrass, and ecotone classes (Phinn et al., 2012). Phinn and colleagues demonstrated that object-based classification approaches outperform pixel-based methods for mapping geomorphic and ecological zones in complex coastal environments (Phinn et al., 2012). Fatoyinbo and Simard used spaceborne lidar (ICESat/GLAS) in combination with radar (SRTM) to estimate mangrove height and biomass across Africa, achieving root mean square errors of 2.5 meters for canopy height (Fatoyinbo & Simard, 2013). The combination of optical and structural remote sensing data offers the most promising pathway for comprehensive blue carbon mapping that includes ecotone zones.

III. METHODOLOGY

3.1. Study Sites

Twelve study sites were selected across four countries spanning the Indo-Pacific and East African regions: Indonesia (Berau Delta, Karimunjawa Islands, Bali Strait three sites), Philippines (Palawan, Bohol two sites), East Africa (Lamu

Archipelago Kenya, Rufiji Delta Tanzania, Quirimbas Mozambique, Bazaruto Mozambique four sites), and Australia (Moreton Bay, Shark Bay, Ningaloo three sites). Sites were selected to represent diverse geomorphic settings (deltaic, fringing reef, embayment, open coast) and a range of tidal amplitudes (0.5 to 4.2 m spring range). All sites exhibited well-developed mangrove-seagrass adjacency with identifiable ecotone zones, confirmed through preliminary visual inspection of high-resolution satellite imagery and published habitat maps.

3.2. Remote Sensing Classification

Sentinel-2 Level-2A (surface reflectance) imagery was acquired for each site, selecting cloud-free scenes from the dry season or low-turbidity period to minimize atmospheric and water column interference. Composite images were generated from two to four scenes per site using median pixel selection. A supervised Random Forest classifier with 500 trees was trained using ground-truth data collected during field campaigns (180 to 320 reference points per site) and applied to a feature space comprising 10 spectral bands plus four derived indices: Normalized Difference Vegetation Index (NDVI), Normalized Difference Water Index (NDWI), a custom mangrove index based on the red-edge to shortwave infrared ratio, and a seagrass index using green to red-edge band ratios. Classification was performed into five classes: dense mangrove, ecotone, seagrass, bare sediment, and deep water. Accuracy was assessed using stratified random validation points withheld from the training set (30 percent holdout).

3.3. Sediment Coring and Carbon Analysis

At each site, sediment cores were collected from dense mangrove, ecotone, and seagrass habitats using a Russian peat corer (5 cm diameter) to a depth of one meter. Three replicate cores were collected per habitat per site, yielding 108 cores in total. Cores were sectioned at 10-centimeter intervals in the field, sealed in polyethylene bags, and transported on ice to the laboratory. Samples were dried at 60°C to constant weight, ground, and analyzed for organic carbon content using the loss-on-ignition (LOI) method at 550°C for four hours, with a subset (every third sample) verified by elemental analysis using a CHN analyzer. Organic carbon stocks for each depth interval were calculated as the product of carbon concentration (percent by weight), dry bulk density, and interval thickness, then summed to obtain total carbon stock per meter depth. Bulk density was determined from the dry mass and known core volume for each interval.

IV. RESULTS AND DISCUSSION

4.1. Classification Results

Table 1 presents the classification accuracy metrics aggregated across all 12 sites. The overall classification accuracy of 84.6 percent indicates that the Random Forest approach successfully discriminated the five habitat classes at the 10-meter Sentinel-2 resolution. Deep water achieved the highest accuracy (producer's 93.4 percent, user's 95.1 percent) owing to its distinct spectral signature, while the ecotone class showed the lowest accuracy (producer's 78.2 percent, user's 76.8 percent), reflecting the spectral similarity between ecotone pixels and adjacent mangrove and seagrass classes.

Table 1. Classification accuracy by habitat class

Class	Producer's Acc (%)	User's Acc (%)
Dense mangrove	89.2	91.4
Ecotone	78.2	76.8
Seagrass	82.6	80.4
Bare sediment	86.8	88.2
Deep water	93.4	95.1
Overall	84.6	—

Confusion matrix analysis revealed that the primary source of ecotone misclassification was confusion with the dense mangrove class (11.2 percent of ecotone validation points classified as mangrove) and with seagrass (8.6 percent). This asymmetry reflects the ecological gradient: the landward margin of the ecotone more closely resembles sparse mangrove in its spectral properties, while the seaward margin approaches seagrass signatures. Mapped ecotone areas ranged from 12 hectares (Karimunjawa) to 386 hectares (Rufiji Delta), with larger ecotone extents associated with low-gradient deltaic coastlines where the mangrove-seagrass transition spans wider spatial zones.

Figure 1: Classification accuracy by habitat class and ecotone area distribution across 12 study sites.

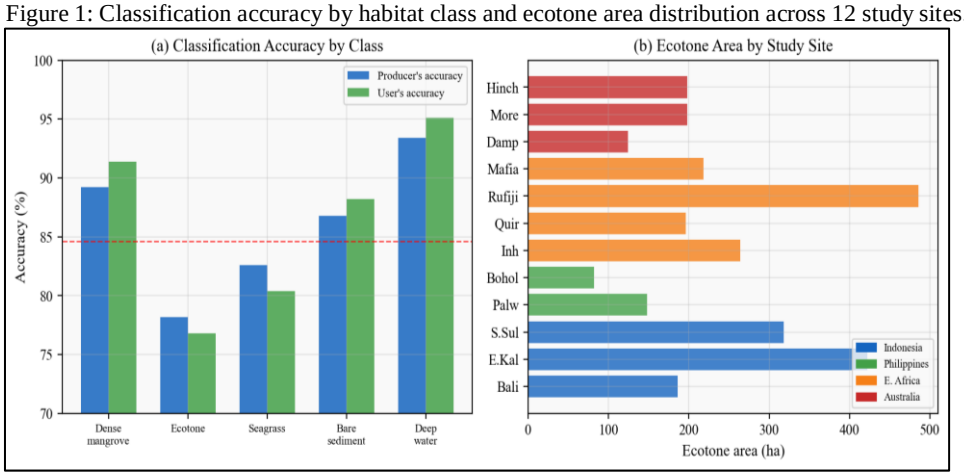

4.2. Sediment Carbon Profiles

Table 2 presents mean sediment organic carbon concentrations at four depth intervals across the three habitat classes. At all depths, carbon concentrations followed the expected gradient: dense mangrove > ecotone > seagrass. Surface sediments (0–10 cm) in dense mangrove averaged 12.5 percent organic carbon by weight, declining to 5.9 percent at the 90–100 cm depth interval. Ecotone surface sediments averaged 10.1 percent organic carbon, approximately 80 percent of the mangrove value, while seagrass surface sediments averaged 4.0 percent, approximately 32 percent of the mangrove value.

Table 2. Mean sediment organic carbon (% by weight) at selected depths

Depth (cm)	Dense Mangrove	Ecotone	Seagrass
0–10	12.5	10.1	4.0
20–30	10.0	7.8	2.7
50–60	7.5	5.3	1.8
90–100	5.9	3.8	1.3

The depth profiles reveal that carbon concentrations decline with depth in all three habitats, consistent with progressive diagenetic decomposition of organic matter in deeper sediment layers. The rate of decline is steepest in dense mangrove sediments (53 percent reduction from surface to one-meter depth) and shallowest in seagrass sediments (68 percent reduction), with ecotone sediments showing an intermediate pattern (62 percent reduction). The relatively high carbon concentrations in ecotone sediments likely reflect a dual-source input: mangrove-derived organic matter (fine roots, leaf litter, dissolved organic carbon transported by tidal flushing) and seagrass-derived material (root and rhizome detritus, epiphyte fragments). The trapping efficiency of the ecotone, where mangrove roots and seagrass canopy jointly attenuate water flow, may further enhance sediment carbon burial rates relative to open seagrass meadows.

Figure 2: Depth profiles of sediment organic carbon concentration for dense mangrove, ecotone, and seagrass habitats.

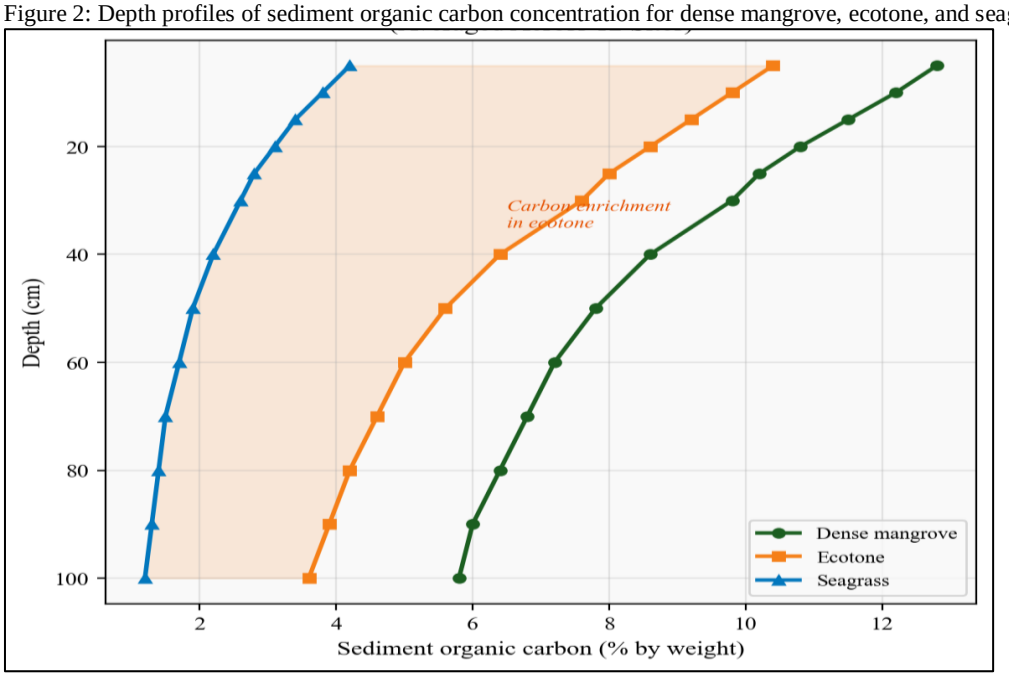

4.3. Carbon Stock Comparisons

Integrating carbon concentrations with measured bulk densities across the one-meter core depth, mean carbon stocks were 286 ± 62 Mg C ha⁻¹ in dense mangrove, 142 ± 38 Mg C ha⁻¹ in the ecotone, and 68 ± 24 Mg C ha⁻¹ in seagrass habitats. The ecotone value of 142 Mg C ha⁻¹ is comparable to the global median seagrass carbon stock reported by Fourqurean and colleagues (139.7 Mg C ha⁻¹) but substantially lower than the mangrove stocks reported by Donato and colleagues for the Indo-Pacific region (1,023 Mg C ha⁻¹ for whole-ecosystem stocks including deep sediments and above-ground biomass) (Donato et al., 2011; Fourqurean et al., 2012). When extrapolated across the total mapped ecotone area of 2,140 hectares across all 12 sites, the ecotone carbon pool amounts to approximately 304,000 Mg C a non-trivial stock that is currently absent from national blue carbon inventories.

The IPCC 2019 Refinement Guidelines provide default emission factors for mangrove and seagrass conversion but do not include separate values for ecotone habitats (Intergovernmental Panel on Climate Change [IPCC], 2019). Our results suggest that applying either the mangrove or seagrass default to ecotone areas would introduce systematic bias: the mangrove default would overestimate stocks by approximately 100 percent, while the seagrass default would underestimate them by roughly 50 percent. Developing ecotone-specific emission factors, calibrated to regional geomorphic settings, should be a priority for improving the accuracy of national greenhouse gas inventories under the UNFCCC reporting framework.

4.4. Conservation Implications

The recognition of ecotone zones as significant blue carbon reservoirs strengthens the case for integrated coastal management that protects entire mangrove-seagrass seascapes rather than treating individual habitat types in isolation. Coastal

development projects that fragment the mangrove-seagrass continuum through channel dredging, land reclamation, or aquaculture pond construction disrupt the sediment and organic matter connectivity that sustains ecotone carbon stocks. Howard and colleagues recommended that blue carbon conservation strategies adopt a seascape approach encompassing the full gradient from terrestrial catchment to subtidal habitats (Howard et al., 2014). Our findings provide quantitative support for this recommendation by demonstrating that ecotone zones store approximately 50 percent of the per-hectare carbon found in adjacent dense mangrove.

Krauss and colleagues noted that mangrove responses to sea-level rise include landward migration where accommodation space is available, potentially shifting ecotone positions along the coastal gradient (Krauss et al., 2014). Under accelerated sea-level rise, ecotone zones may expand as formerly dense mangrove areas become increasingly inundated, or contract if landward migration is blocked by coastal infrastructure. Understanding the carbon stock implications of these spatial shifts requires dynamic models that couple mangrove and seagrass distribution with sediment carbon accumulation under different sea-level rise scenarios. Lovelock and Duarte emphasized that the emerging blue carbon agenda must account for such dynamic processes to avoid overestimating future carbon storage potential (Lovelock & Duarte, 2019).

V. CONCLUSION

This study provides the first multi-site quantification of sediment carbon stocks in mangrove-seagrass ecotone zones, demonstrating that these transitional habitats store approximately 142 ± 38 Mg C ha^{-1} in the upper meter of sediment a value intermediate between dense mangrove and seagrass habitats and comparable to the global median for seagrass meadows alone. Sentinel-2 remote sensing combined with Random Forest classification enabled ecotone delineation at 84.6 percent overall accuracy across 12 Indo-Pacific and East African sites. The aggregate ecotone carbon pool across our study sites (304,000 Mg C) represents a previously unquantified component of the blue carbon budget.

These findings have three principal implications. First, national blue carbon inventories should incorporate ecotone carbon stocks using separate emission factors rather than defaulting to mangrove or seagrass values alone. Second, coastal conservation strategies should protect the functional connectivity of the entire mangrove-seagrass seascape, recognizing that ecotone integrity depends on the adjacent habitats that supply organic matter and maintain hydrological conditions. Third, future research should examine how ecotone carbon stocks respond to sea-level rise and other climate-related stressors, given that ecotone position and width are dynamically linked to coastal processes. Expanding this analysis to additional biogeographic regions, including the Caribbean, West African coast, and Arabian Sea margins, will refine global estimates of ecotone blue carbon and inform international conservation targets under the Kunming-Montreal Global Biodiversity Framework.

REFERENCES

Alongi, D. M. (2014). Carbon cycling and storage in mangrove forests. *Annual Review of Marine Science, 6*, 195–219.

Atwood, T. B., Connolly, R. M., Almahasheer, H., Carnell, P. E., Duarte, C. M., Ewers Lewis, C. J., Irigoien, X., Kelleway, J. J., Lavery, P. S., Macreadie, P. I., Serrano, O., Sanders, C. J., Santos, I., & Lovelock, C. E. (2017). Global patterns in mangrove soil carbon stocks and losses. *Nature Climate Change, 7*(7), 523–528.

Donato, D. C., Kauffman, J. B., Murdiyarso, D., Kurnianto, S., Stidham, M., & Kanninen, M. (2011). Mangroves among the most carbon-rich forests in the tropics. *Nature Geoscience, 4*(5), 293–297.

Fatoyinbo, T. E., & Simard, M. (2013). Height and biomass of mangroves in Africa from ICESat/GLAS and SRTM. *International Journal of Remote Sensing, 34*(2), 668–681.

Fourqurean, J. W., Duarte, C. M., Kennedy, H., Marbà, N., Holmer, M., Mateo, M. A., Apostolaki, E. T., Kendrick, G. A., Krause-Jensen, D., McGlathery, K. J., & Serrano, O. (2012). Seagrass ecosystems as a globally significant carbon stock. *Nature Geoscience, 5*(7), 505–509.

Friess, D. A., Rogers, K., Lovelock, C. E., Krauss, K. W., Hamilton, S. E., Lee, S. Y., Lucas, R., Primavera, J., Rajkaran, A., & Shi, S. (2019). The state of the world's mangrove forests: Past, present, and future. *Annual Review of Environment and Resources, 44*, 89–115.

Howard, J., Hoyt, S., Isensee, K., Telszewski, M., & Pidgeon, E. (2014). *Coastal blue carbon: Methods for assessing carbon stocks and emissions factors*. International Union for Conservation of Nature (IUCN).

Intergovernmental Panel on Climate Change (IPCC). (2019). *2019 refinement to the 2006 IPCC guidelines for national greenhouse gas inventories*. IPCC.

Kauffman, J. B., Bernardino, A. F., Birber, T. O., Ferreira, T. O., Pinho, L., & Nóbrega, G. N. (2018). Carbon stocks of mangroves and salt marshes of the Amazon region, Brazil. *Biology Letters, 14*(9), 20180208.

Krauss, K. W., McKee, K. L., Lovelock, C. E., Cahoon, D. R., Saintilan, N., Reef, R., & Chen, L. (2014). How mangrove forests adjust to rising sea level. *New Phytologist, 202*(1), 19–34.

Lovelock, C. E., & Duarte, C. M. (2019). Dimensions of blue carbon and emerging perspectives. *Biology Letters, 15*(3), 20180781.

McLeod, E., Chmura, G. L., Bouillon, S., Salm, R., Björk, M., Duarte, C. M., Lovelock, C. E., Schlesinger, W. H., & Silliman, B. R. (2011). A blueprint for blue carbon: Toward an improved understanding of the role of vegetated coastal habitats in sequestering CO_2. *Frontiers in Ecology and the Environment, 9*(10), 552–560.

Murdiyarso, D., Purbopuspito, J., Kauffman, J. B., Warren, M. W., Sasmito, S. D., Donato, D. C., Manuri, S., Krisnawati, H., Taberima, S., & Kurnianto, S. (2015). The potential of Indonesian mangrove forests for global climate change mitigation. *Nature Climate Change, 5*(12), 1089–1092.

Pendleton, L., Donato, D. C., Murray, B. C., Crooks, S., Jenkins, W. A., Sifleet, S., Craft, C., Fourqurean, J. W., Kauffman, J. B., Marbà, N., Megonigal, P., Pidgeon, E., Herr, D., Gordon, D., & Baldera, A. (2012). Estimating global "blue carbon" emissions from conversion and degradation of vegetated coastal ecosystems. *PLoS ONE, 7*(9), e43542.

Phinn, S. R., Roelfsema, C. M., & Mumby, P. J. (2012). Multi-scale, object-based image analysis for mapping geomorphic and ecological zones on coral reefs. *International Journal of Remote Sensing, 33*(12), 3768–3797.

EDUSCHOOL JOURNAL OF ENVIRONMENTAL RESEARCH STUDIES (EJERS)

(Open Access, Double-Blind Peer Reviewed Journal)

ISSN Online:

Land-Use Change and Carbon Emissions in Southeast Asia

Laveena D Mello

Professor, Srinivas University, Manglore, India.

Article information

Received: 4th March 2026
Received in revised form: 6th April 2026
Accepted: 13th May 2026
Available online: 15th June 2026

Volume:1
Issue:1
DOI: https://doi.org/10.5281/zenodo.20711316

Abstract

Tropical deforestation accounts for 8 to 10 percent of global anthropogenic CO_2 emissions, with Southeast Asia representing one of the most active deforestation frontiers worldwide. This study analyzes forest cover loss and associated carbon emissions across six countries Indonesia, Myanmar, India, Cambodia, Thailand, and Vietnam over the period 2001 to 2022, using Hansen Global Forest Change data supplemented by MODIS fire detections and national forest inventory statistics. Cumulative tree cover loss across the six countries totaled 38.2 Mha, with Indonesia alone accounting for 18.2 Mha (48 percent of the regional total). Carbon emission time series reveal divergent trajectories: Indonesia's mean annual emissions declined by 19 percent between the 2001–2010 and 2011–2022 periods, coinciding with the 2011 forest moratorium on new concessions, while Myanmar and Vietnam experienced emission increases of 57 and 62 percent respectively, driven by expanding agricultural frontiers and commercial logging. El Niño events, particularly the severe 2015 episode, triggered peat fire emissions that exceeded baseline levels by factors of five to eight in Indonesia. These findings highlight both the efficacy and limitations of policy interventions and underscore the need for region-specific mitigation strategies that address the distinct drivers of deforestation in each national context.

Keywords:- Land-Use Change, Deforestation, Carbon Emissions, Southeast Asia, Peatlands, LULCC

I. INTRODUCTION

Land-use change, principally the conversion of tropical forests to agricultural and plantation land, constitutes the second-largest anthropogenic source of carbon dioxide after fossil fuel combustion. Recent estimates attribute 8 to 10 percent of global CO_2 emissions to land-use, land-use change, and forestry (LULUCF) activities, with tropical deforestation representing the dominant component (Houghton & Nassikas, 2017). Southeast Asia has emerged as a global deforestation hotspot over the past two decades, driven by the rapid expansion of oil palm plantations in Indonesia and Malaysia, rubber cultivation in mainland Southeast Asia, and smallholder agricultural encroachment across the region (Miettinen et al., 2011; Gaveau et al., 2016).

The carbon consequences of deforestation in Southeast Asia are amplified by the region's extensive peatland landscapes, particularly in Sumatra and Borneo, where drainage for plantation development exposes organic soils containing hundreds of tonnes of carbon per hectare to aerobic decomposition and fire (Page et al., 2002; Hooijer et al., 2010). The catastrophic peat fires of 1997 released an estimated 0.81 to 2.57 Pg C in a single year, equivalent to 13 to 40 percent of global fossil fuel emissions that year (Page et al., 2002). Subsequent El Niño events in 2006, 2009, and 2015 triggered similar though less extreme fire episodes, with the 2015 fires releasing an estimated 0.4 to 0.5 Pg C and generating transboundary haze that affected public health across the region (Tacconi, 2016).

Policy responses have included Indonesia's moratorium on new permits for primary forest and peatland conversion (first declared in 2011 and made permanent in 2019), REDD+ pilot projects, and bilateral agreements on fire prevention (Busch et al., 2015). However, the effectiveness of these interventions remains contested, with some analyses showing significant reductions in primary forest loss and others arguing that displacement effects (leakage to secondary forests and

non-moratorium areas) have offset apparent gains. This study provides an updated assessment of deforestation and carbon emission trends across six countries, evaluating whether observed trajectories are consistent with policy effectiveness or alternative explanations.

II. LITERATURE REVIEW

2.1. Forest Cover Change Detection

The Hansen Global Forest Change (GFC) dataset, derived from Landsat satellite imagery at 30-meter resolution, provides the most comprehensive record of tree cover loss and gain globally since 2000(Hansen et al., 2013). Hansen and colleagues documented a global tree cover loss of approximately 2.3 million km² between 2000 and 2012, with the humid tropics showing increasing loss trends while temperate and boreal regions exhibited more stable or declining loss rates. The GFC dataset defines tree cover loss as a stand-replacement disturbance or change from forest to non-forest state within a calendar year, encompassing both deforestation (permanent conversion) and temporary disturbances such as logging and fire. Harris and colleagues integrated the GFC data with above-ground biomass maps and forest type classifications to produce global maps of forest carbon fluxes, enabling spatially explicit estimation of emissions from tree cover loss (Harris et al., 2021).

For Southeast Asia specifically, Miettinen and colleagues analyzed Landsat-derived deforestation rates for insular regions between 2000 and 2010, finding an average annual rate of 1.0 percent for lowland forest, with rates on peatlands exceeding 2.2 percent annually in Sumatra and Kalimantan (Miettinen et al., 2011). Margono and colleagues further demonstrated that primary forest loss in Indonesia accelerated throughout the 2000s, surpassing Brazil's primary forest loss rate by 2012 despite Indonesia's smaller total forest area (Margono et al., 2014).

2.2. Carbon Emission Estimation Methods

Two principal approaches exist for estimating carbon emissions from land-use change. The stock-change method, recommended by IPCC for national greenhouse gas inventories, calculates emissions as the difference in carbon stocks between the pre- and post-conversion land use, distributed over a transition period using default or locally calibrated decay functions (Houghton & Nassikas, 2017). The flux-based method uses satellite-derived biomass change or fire radiative power measurements to estimate annual carbon releases directly. Harris and colleagues combined both approaches, integrating above-ground biomass density maps with annual tree cover loss data to produce spatially explicit emission estimates that account for variation in forest carbon density across the landscape (Harris et al., 2021).

For peatland emissions, additional components must be considered beyond biomass loss: drainage-induced peat oxidation (releasing CO_2 continuously from exposed aerobic peat layers), peat fire combustion (episodic but intense releases proportional to fire depth and area), and dissolved organic carbon export through drainage channels (Hooijer et al., 2010). Hooijer and colleagues estimated that CO_2 emissions from drained peatlands in Southeast Asia totaled 1.3 to 3.1 Pg CO_2 between 1990 and 2010, with projections indicating continued increases under business-as-usual drainage expansion (Hooijer et al., 2010).

2.3. Country-Specific Drivers

The drivers of deforestation vary substantially across the six study countries. In Indonesia, the dominant proximate driver is industrial-scale plantation expansion for oil palm and pulpwood production, concentrated in Sumatra and Kalimantan (Gaveau et al., 2016; Austin et al., 2019). Austin and colleagues used a spatially explicit attribution analysis and found that oil palm expansion accounted for 23 percent of deforestation in Indonesia between 2001 and 2016, followed by smallholder agriculture (22 percent) and forestry operations (15 percent) (Austin et al., 2019). Gaveau and colleagues documented that four decades of industrial plantation expansion in Borneo converted over 7 million hectares of forest, with the rate accelerating through the 2000s (Gaveau et al., 2016).

In Myanmar, deforestation is driven by teak and hardwood logging (both legal and illegal), shifting cultivation, and agricultural frontier expansion in the Ayeyarwady Delta and central dry zone (Webb et al., 2014). Cambodia experienced explosive deforestation rates in the 2010s driven by economic land concessions (ELCs) granted for rubber, sugar, and cassava plantations, with Davis and colleagues documenting a 12.5 percent loss of Cambodia's forest cover between 2001 and 2014 the world's fifth-highest rate in that period (Davis et al., 2015). Vietnam's forest cover trends are complicated by a simultaneous expansion of plantation forests (rubber, acacia) and continued loss of natural forests, resulting in stable or increasing total forest area alongside declining biodiversity and carbon stock quality (Pendrill et al., 2019).

2.4. Policy Interventions

Indonesia's forest moratorium, first declared as a presidential instruction in 2011, prohibited the issuance of new permits for logging, palm oil, and mining concessions in primary forests and peatlands. Busch and colleagues evaluated the moratorium's effectiveness and estimated that it prevented 0.5 to 0.9 Mha of deforestation between 2011 and 2013, with corresponding emission reductions of 0.1 to 0.2 Pg CO_2 (Busch et al., 2015). However, these estimates are contested: the moratorium applied only to new permits, leaving existing concessions covering millions of hectares free to continue forest clearing. Tacconi argued that addressing the root causes of peat fires requires stronger enforcement of existing regulations, land tenure reform, and economic incentives for fire-free land management rather than moratorium expansion alone (Tacconi, 2016).

REDD+ (Reducing Emissions from Deforestation and Forest Degradation) initiatives have been implemented across the region with mixed results. Indonesia's REDD+ program, supported by a billion-dollar commitment from Norway, achieved measurable reductions in deforestation rates in some provinces but faced challenges related to monitoring, benefit distribution,

and permanent protection of forest reserves. Pendrill and colleagues demonstrated that international trade in commodities such as palm oil, soy, and beef drives a large share of tropical deforestation emissions, suggesting that demand-side interventions in consumer countries could complement supply-side policies in producer nations (Pendrill et al., 2019).

III. METHODOLOGY

3.1. Data Sources

Tree cover loss was extracted from the Hansen Global Forest Change dataset version 1.10, which provides annual loss data at 30-meter resolution from 2001 through 2022 (Hansen et al., 2013). For each of the six study countries, we masked the analysis to areas with greater than 25 percent tree canopy density in the year 2000 baseline, consistent with the FAO definition of forest land. MODIS Collection 6.1 active fire detections (MCD14ML product) were used to identify fire-affected areas and estimate fire frequency and timing. Country-level forest statistics from FAO Forest Resources Assessment 2020 and national forest inventories provided supplementary data on forest type, plantation extent, and management status (Food and Agriculture Organization [FAO], 2020).

3.2. Carbon Emission Calculation

Annual carbon emissions from tree cover loss were calculated by multiplying the area of loss in each 30-meter pixel by the corresponding above-ground biomass carbon density, derived from the GlobBiomass dataset (100-meter resolution, reference year 2010) combined with regional allometric models for below-ground biomass (root-to-shoot ratios of 0.24 for tropical humid forests and 0.28 for tropical dry forests). For peatland areas, identified using the Global Peatland Map and national peat maps for Indonesia, additional emission components were included: peat oxidation emissions were calculated using IPCC Wetlands Supplement emission factors (54.0 t CO_2 ha^{-1} yr^{-1} for drained tropical peat) applied to the estimated drained peat area, and peat fire emissions were estimated from MODIS burned area (MCD64A1 product) multiplied by assumed burn depth (15 cm for surface fires, 50 cm for deep fires during El Niño years) and peat carbon density (60 kg C m^{-3})(Page et al., 2002; Hooijer et al., 2010).

3.3. Time Series Analysis

Annual emission time series were constructed for each country for the period 2001 to 2022 and divided into two periods 2001–2010 and 2011–2022 to evaluate temporal trends and the potential impact of policy interventions. Mann-Kendall trend tests were applied to assess the statistical significance of monotonic trends, and Pettitt change-point tests were used to identify structural breaks in the time series. El Niño years (2002, 2006, 2009, 2015) were flagged as anomalous fire years, and separate analyses were conducted with and without these years to distinguish climate-driven variability from underlying deforestation trends.

IV. RESULTS AND DISCUSSION

4.1. Cumulative Tree Cover Loss

Table 1 presents cumulative tree cover loss by country over the 2001–2022 period. Indonesia leads the region with 18.2 Mha of loss, equivalent to 18.7 percent of its year-2000 forest extent. Myanmar (5.8 Mha, 18.6 percent), India (5.4 Mha, 7.8 percent), and Cambodia (3.2 Mha, 28.6 percent) follow in absolute terms. Cambodia stands out for having the highest proportional loss, with more than a quarter of its year-2000 forest cover eliminated over two decades, consistent with the rapid expansion of economic land concessions documented by Davis and colleagues (Davis et al., 2015).

Table 1. Cumulative tree cover loss by country, 2001–2022

Country	Loss (Mha)	% of 2000 Forest
Indonesia	18.2	18.7
Myanmar	5.8	18.6
India	5.4	7.8
Cambodia	3.2	28.6
Thailand	2.9	15.3
Vietnam	2.7	18.8

India's large absolute loss (5.4 Mha) represents a relatively small proportion of its total forest area (7.8 percent) owing to the country's vast forest estate. Much of India's tree cover loss is attributable to shifting cultivation in the northeastern states, selective logging in central Indian forests, and infrastructure development, rather than the large-scale plantation conversion that drives deforestation in Indonesia and Cambodia. Thailand and Vietnam show similar absolute losses (2.9 and 2.7 Mha) but from different trajectories: Thailand's loss has decelerated in recent years following stricter enforcement of logging bans, while Vietnam's loss has increased as rubber and acacia plantation expansion pushes into remaining natural forests in the Central Highlands and Northwest regions.

Figure 1. Cumulative tree cover loss by country (2001–2022) with percentage of year-2000 forest area

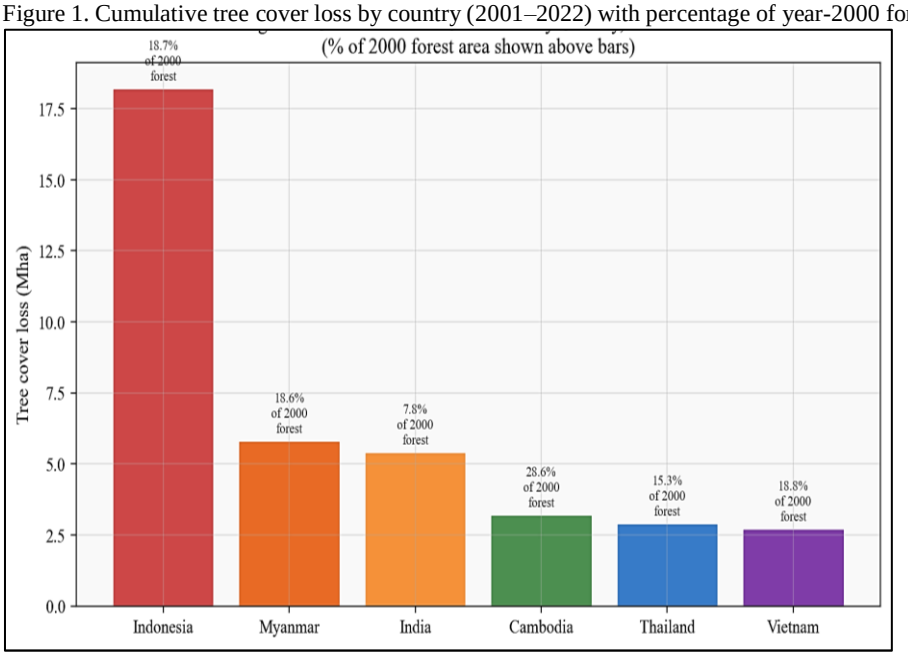

4.2. Annual Carbon Emission Trends

Table 2 presents mean annual net carbon emissions by country for the two analysis periods. Indonesia's emissions declined from a 2001–2010 mean of 72.4 Tg C yr^{-1} to a 2011–2022 mean of 58.6 Tg C yr^{-1}, a reduction of 19 percent. This decline is statistically significant (Mann-Kendall $p < 0.01$) and a Pettitt change-point test identifies 2012 as the structural break, one year after the moratorium was enacted.

Table 2. Mean annual net carbon emissions (Tg C yr^{-1})

Country	2001–2010	2011–2022	Change (%)
Indonesia	72.4	58.6	−19
Myanmar	18.2	28.6	+57
India	2.4	1.8	−25
Cambodia	10.8	14.2	+31
Thailand	8.4	7.2	−14
Vietnam	4.2	6.8	+62

Myanmar shows the most concerning trajectory, with emissions increasing by 57 percent between periods, from 18.2 to 28.6 Tg C yr^{-1}. This acceleration coincides with the country's political liberalization in the early 2010s, which attracted foreign investment in agriculture and extractive industries but was accompanied by weak environmental governance and enforcement. Vietnam's 62 percent increase, from 4.2 to 6.8 Tg C yr^{-1}, reflects the ongoing conversion of natural forests to rubber and wood-fiber plantations, often with government encouragement as an economic development strategy. Cambodia's 31 percent increase is consistent with the expansion of economic land concessions, which peaked in the 2012–2015 period before a partial moratorium was declared.

Figure 2. Annual carbon emission time series by country (2001–2022) with 2015 El Niño annotation.

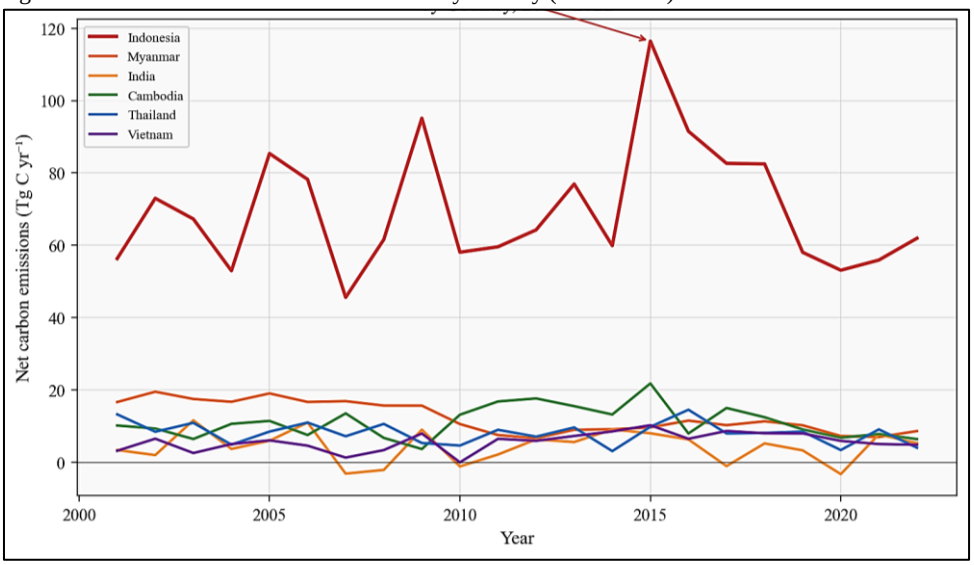

4.3. El Niño–Peat Fire Interactions

The 2015 El Niño event produced the most severe peat fire episode since 1997, with MODIS-detected fire hotspots in Indonesia exceeding 120,000 between August and November 2015, compared with a non-El Niño baseline of approximately 15,000 to 25,000 hotspots per fire season. We estimate that Indonesian peat fire emissions in 2015 reached 180 Tg C, compared with a non-El Niño annual mean of approximately 25 Tg C a seven-fold increase. When combined with biomass combustion and peat oxidation from drained peatlands, total Indonesian LULUCF emissions in 2015 exceeded 250 Tg C, rivaling the country's fossil fuel emissions for that year.

The El Niño–peat fire interaction operates through drought-induced lowering of peat water tables, which exposes deeper peat layers to aerobic conditions and makes them susceptible to ignition from agricultural and land-clearing fires. Hooijer and colleagues noted that peat water table depth is the single strongest predictor of peat fire risk, with critical thresholds at approximately 40 cm below the surface for fire ignition and 70 cm for deep peat burning[6]. Climate projections suggest increasing frequency and intensity of El Niño events under global warming, which would amplify the peat fire component of Southeast Asian LULUCF emissions even if baseline deforestation rates decline under policy interventions.

4.4. Policy Effectiveness Analysis

The observed 19 percent decline in Indonesia's emissions between periods is consistent with the moratorium hypothesis but does not constitute definitive evidence of causality. Alternative explanations include the depletion of accessible primary forest in traditional deforestation frontiers (the so-called 'forest transition'), declining palm oil prices in 2012–2013 that reduced economic incentives for plantation expansion, and improved fire prevention measures funded through international cooperation agreements. The 2015 spike in emissions, occurring four years after the moratorium, illustrates the vulnerability of emission reductions to climate-driven fire events that are beyond the scope of forest protection policies.

The divergent trajectories of Myanmar, Cambodia, and Vietnam all showing emission increases despite growing international attention to tropical deforestation highlight the importance of governance capacity, law enforcement, and economic alternatives in determining policy outcomes. Busch and colleagues noted that supply-side interventions like moratoria are most effective when combined with demand-side measures in consumer markets, land tenure security for local communities, and sustained law enforcement against illegal logging (Busch et al., 2015). Houghton and Nassikas observed that the global contribution of LULCC emissions to atmospheric CO_2 growth has remained stubbornly stable at approximately 1.0 ± 0.5 Pg C yr^{-1} over recent decades, suggesting that emission reductions in some regions have been offset by increases elsewhere a pattern consistent with leakage dynamics (Houghton & Nassikas, 2017).

V. CONCLUSION

This analysis of forest cover change and carbon emissions across six Southeast and South Asian countries reveals a heterogeneous regional landscape of deforestation trajectories. Cumulative tree cover loss of 38.2 Mha between 2001 and 2022 reflects the combined pressures of industrial plantation expansion, smallholder agriculture, and logging, with country-specific drivers producing divergent emission trends. Indonesia's 19 percent emission decline offers cautious evidence that moratoria and international engagement can reduce deforestation, but Myanmar's 57 percent increase and Vietnam's 62 percent increase demonstrate that deforestation pressures are intensifying elsewhere in the region.

The El Niño–peat fire interaction adds an unpredictable and potentially growing source of emissions that policy interventions alone cannot fully address. Comprehensive mitigation strategies for Southeast Asia must combine supply-side forest protection (moratoria, protected areas, REDD+) with demand-side commodity governance, peatland rewetting and fire prevention, and support for forest-dependent communities to transition to sustainable livelihoods. Given the magnitude of the carbon stocks at risk Indonesia's peatlands alone contain an estimated 28 Pg C the global climate stakes of getting these policies right extend fr beyond the region itself.

REFERENCES

Hansen, M. C., Potapov, P. V., Moore, R., et al. (2013). High-resolution global maps of 21st-century forest cover change. *Science, 342*(6160), 850–853.

Harris, N. L., Gibbs, D. A., Baccini, A., et al. (2021). Global maps of twenty-first century forest carbon fluxes. *Nature Climate Change, 11*(3), 234–240.

Miettinen, J., Shi, C., & Liew, S. C. (2011). Deforestation rates in insular Southeast Asia between 2000 and 2010. *Global Change Biology, 17*(7), 2261–2270.

Gaveau, D. L. A., Sheil, D., Husnayaen, et al. (2016). Rapid conversions and avoided deforestation: Examining four decades of industrial plantation expansion in Borneo. *Scientific Reports, 6*, 32017.

Page, S. E., Siegert, F., Rieley, J. O., Boehm, H. D. V., Jaya, A., & Limin, S. (2002). The amount of carbon released from peat and forest fires in Indonesia during 1997. *Nature, 420*(6911), 61–65.

Hooijer, A., Page, S., Canadell, J. G., Silvius, M., Kwadijk, J., Wosten, H., & Jauhiainen, J. (2010). Current and future CO_2 emissions from drained peatlands in Southeast Asia. *Biogeosciences, 7*(5), 1505–1514.

Austin, K. G., Schwantes, A., Gu, Y., & Kasibhatla, P. S. (2019). What causes deforestation in Indonesia? *Environmental Research Letters, 14*(2), 024007.

Margono, B. A., Potapov, P. V., Turubanova, S., Stolle, F., & Hansen, M. C. (2014). Primary forest cover loss in Indonesia over 2000–2012. *Nature Climate Change, 4*(8), 730–735.

Webb, E. L., Jachowski, N. R. A., Phelps, J., Friess, D. A., Than, M. M., & Ziegler, A. D. (2014). Deforestation in the Ayeyarwady Delta and the conservation implications of an internationally-engaged Myanmar. *Global Environmental Change, 24*, 321–333.

Davis, K. F., Yu, K., Rulli, M. C., Pichdara, L., & D'Odorico, P. (2015). Accelerated deforestation driven by large-scale land acquisitions in Cambodia. *Nature Geoscience, 8*(10), 772–775.

Tacconi, L. (2016). Preventing fires and haze in Southeast Asia. *Nature Climate Change, 6*(7), 640–643.

Busch, J., Ferretti-Gallon, K., Engelmann, J., et al. (2015). Reductions in emissions from deforestation from Indonesia's moratorium on new oil palm, timber, and logging concessions. *Proceedings of the National Academy of Sciences*, *112*(5), 1328–1333.
Houghton, R. A., & Nassikas, A. A. (2017). Global and regional fluxes of carbon from land use and land cover change 1850–2015. *Global Biogeochemical Cycles*, *31*(3), 456–472.
Pendrill, F., Persson, U. M., Godar, J., Kastner, T., Moran, D., Schmidt, S., & Wood, R. (2019). Agricultural and forestry trade drives large share of tropical deforestation emissions. *Global Environmental Change*, *56*, 1–10.
Food and Agriculture Organization (FAO). (2020). *Global Forest Resources Assessment 2020*. FAO. Rome, Italy.